



Contents lists available at ScienceDirect

## International Journal of Plasticity

journal homepage: [www.elsevier.com/locate/ijplas](http://www.elsevier.com/locate/ijplas)

# Multiscale stress and strain statistics in the deformation of polycrystalline alloys

Jingwei Chen, Zifan Wang, Alexander M. Korsunsky<sup>\*</sup>

MBLEM, Department of Engineering Science, University of Oxford, Parks Road, Oxford OX1 3PJ, United Kingdom

## ARTICLE INFO

## Keywords:

Finite element method  
Representative volume element  
Multiscale analysis  
Stress and strain statistics  
Strain inhomogeneity

## ABSTRACT

Multiscale stresses and strains in polycrystalline metals are always inhomogeneous. In this study, a rate-independent crystal plasticity formulation was implemented for a cubic representative volume element (RVE) of an fcc polycrystal generated by 3D Delaunay tessellation. Multiple realizations were generated with crystallographic orientation permutations and different grain morphologies in order to investigate the statistical distribution of stress, elastic lattice strain and total strain at the macro-, meso- and micro-scale. Macroscopically, at 1.55% total strain (elasto-plastic deformation), the overall stress statistics among different RVEs were observed to follow a normal distribution, whose profile shape is affected by the parameters that describes the lognormal grain size distribution. On the mesoscale, the orientation-specific elastic strains were accurately reproduced via the use of diffraction post-processing and validated by neutron diffraction data for a polycrystalline alloy. Microscopically, the local elastic strains (and hence stresses) universally follow a normal distribution, while plastic strains follow a lognormal probability distribution. Reliable knowledge of the statistical distributions of stresses and strains give new guidance for the determination of the minimum RVE size. The above finding reveals the nature of stress and strain inhomogeneity at multiple scales and emphasizes the fact that the dispersion of local stress and strain is much larger than that of the macroscopic average. The statistical analysis of stress and strain distribution at multiple scales provide further rich insights into the connection between microstructure and mechanical properties under monotonic and cyclic loading.

## 1. Introduction

In polycrystalline metallic materials such as nickel-base superalloys, the deformation response in both elastic and plastic regimes is highly anisotropic (Chen et al., 2020). Depending on their crystallographic orientation with respect to the loading axis, and also depending on the immediate neighbourhood, grains deform to different extents to carry disparate magnitudes of stress under different applied loads, giving rise to heterogeneous stress fields between adjacent grains and within individual grains. Alongside the anisotropy of stiffness and yield resistance of single crystals, the polycrystal grain morphology (grain shapes and sizes) are also important constitutive aspects of the microstructure of polycrystalline aggregates (Farooq et al., 2020). In order to conduct rational and reliable experimental and numerical investigations of the behaviour of polycrystalline materials with complex microstructure, it is essential to

<sup>\*</sup> Corresponding author.

E-mail addresses: [jingwei.chen@eng.ox.ac.uk](mailto:jingwei.chen@eng.ox.ac.uk) (J. Chen), [zifan.wang@exeter.ox.ac.uk](mailto:zifan.wang@exeter.ox.ac.uk) (Z. Wang), [alexander.korsunsky@eng.ox.ac.uk](mailto:alexander.korsunsky@eng.ox.ac.uk) (A.M. Korsunsky).

<https://doi.org/10.1016/j.ijplas.2022.103260>

Received 24 September 2021; Received in revised form 3 February 2022; Accepted 12 February 2022

Available online 14 February 2022

0749-6419/© 2022 The Authors. Published by Elsevier Ltd. This is an open access article under the CC BY license (<http://creativecommons.org/licenses/by/4.0/>).

obtain statistical descriptions of the crystallographic orientation and grain morphology within the material body, and establish their effects on the overall mechanical response of the material.

Until the early 1980s, the modelling of elastoplastic deformation mainly relied on phenomenological formulations at the macroscopic level. Continuum level models neglect the microstructural representation of the heterogeneous nature of the materials, and hence are incapable of providing a reliable reproduction of the deformation process when the relevant length scale goes down to micrometres. Since then, many studies were carried out to establish the foundation of computational plasticity frameworks based on crystal slip (Peirce et al., 1982, 1983). At that time, the vast majority of crystal plasticity simulations were applied to simulate the anisotropic deformation behaviour of single crystal or bicrystals, due to the limitations of computing power. The modelling of polycrystals has become possible and increasingly popular with the development of high-performance computing. Over the past 20 years, researchers have proposed various methods to improve the formulation and implementation of polycrystal plasticity theory (Sarma and Dawson, 1996; Diard et al., 2005; Daoud et al., 2015; Kotha et al., 2019). The most widely used modelling approaches among them are self-consistent (SC) and finite element (FE) based methodologies that include empirically or physically based elastoplastic crystal slip constitutive equations and a detailed representation of microstructure. The implementation of crystal plasticity formulations within the FE framework is referred to as crystal plasticity finite-element (CPFE) methods.

CPFE method can be employed at microscopic and macroscopic scales (Cheong and Busso, 2004; Song et al., 2010). Microscopically, it is widely used to simulate the inter- and intra-grain mechanical behaviour where the contact and boundary conditions are difficult to control or monitor in the experiment. On the macroscopic side, CPFE method mostly utilized in the fields of large-scale forming and texture simulations, where appropriate homogenization schemes are required to represent the phase and texture of the materials under study. This can be achieved by employing the concept of a representative volume element (RVE). RVE is a powerful tool for modelling the effect of micro- and mesoscale heterogeneities on the overall mechanical response of components at the macroscopic level. So far, several definitions and determination methods of RVE have been proposed for different purposes. One of the most commonly used definitions in the literature introduced by Hill (1963) states that an RVE must include a sufficient number of micro-heterogeneities (grains, inclusions, voids, etc.) to obtain the effective properties of heterogeneous materials. The meaning of this statement is twofold: (a) all possible microstructural configurations must be statistically described and (b) the mechanical behaviour of RVE should be correct independently of the boundary condition type. A more explicit definition was proposed by Drugan and Willis (1996) who define RVE as the smallest material volume within components that provides a sufficiently accurate representation of the mean constitutive response. This approach is based on the idea of homogenization for an infinite medium and does not consider the fluctuations of the effective properties over finite domains. Kanit et al. (2003) added statistical consideration to the concept of RVE. Based on Kanit's definition, one single RVE is not enough to get an accurate estimation of effective properties, while a sufficient number of realizations should be simulated to obtain a desired precision for the estimation. This appears to be the first approach that uses multiple realizations and adopts a statistical procedure to analyse the results.

The above review of various definitions of RVE suggests that there has been no systematic quantitative criterion proposed so far for the determination of RVE. As a consequence, the element size used by one author may not be suitable for the research performed by another, leading to some confusion when determining the size of RVE. Although there is a large diversity of criteria used by different researchers, some common considerations are well accepted. The RVE size should be large enough to contain sufficient information about material microstructure in order to be considered as representative, on the other hand, and it should be computationally efficient and hence small enough with regard to the macroscopic dimensions (Trias et al., 2006). While considering the process of RVE determination, the question of stability is always of interest and importance. The mechanical response of RVE can be influenced by statistical size effects caused by uncertainty arising from a poor choice of samples. Such effects can be controlled by increasing the number of realizations to reduce statistical uncertainty. Accordingly, statistical-numerical RVE determination techniques were proposed over the past 15 years. Kanit et al. (2003) created a general framework for RVE determination based on the correlation of numbers of realizations and relative error for linear elastic properties. Gitman et al. (2007) employed the same RVE determination procedure to deal with non-linear material behaviour, but was still based on a very small number of realizations that cannot be statistically representative in the case of highly non-linear mechanical response such as plastic slip. Furthermore, this approach does not quantitatively reproduce how effective properties vary between different realizations. To the best of the authors' knowledge, there is no report providing a mathematical description of the distribution of effective properties among a sufficient number of nominally identical RVEs. While a considerable number of studies has concentrated on the convergence of the macroscopic average properties (e.g. homogenized response), comparatively less attention has been paid to the *statistical distributions* of the local mechanical behaviour within RVE. Furthermore, failure in polycrystalline alloys under cyclic loading frequently originate in highly localized fields where intergranular and intragranular strain and stress dominate. Most failure criteria are extremely sensitive to the existence of stress concentration owing to inclusions or triple points that often have a much smaller influence on the homogenized response, as previously discussed for several heterogeneous systems (Bilger et al., 2005; Dautriat et al., 2011; Lim et al., 2019). Local plastic slip distributions have been widely studied and it is well known that they follow an exponential distribution within the RVE, and an extreme value distribution when comparing the maxima of several RVEs (Jiang et al., 2013; Shimokawa et al., 2014; Chen et al., 2021). Therefore, the frameworks for RVE determination based only on the macroscopic average properties are usually not valid, hence more attempts should be made to investigate the mechanical behaviour at the mesoscopic and microscopic scales along with the attendant statistics.

The inhomogeneous nature of strain and stress distribution has led to the concept of three types of stresses which describe the spatial variation over different length scales. Type I stresses are nearly homogeneous across macroscopic dimensions. Such stresses can be evaluated using the average effects over many grains of RVE without consideration of the behaviour of individual grain. This is in contrast to Type II or mesoscopic stresses which equilibrate over grain scale. It can be calculated from orientation-dependent lattice strain via X-ray diffraction (Statnik et al., 2020) and neutron diffraction (Wang et al., 2020a, 2020b) measurement. Type III stresses, on

the other hand, vary at the sub-grain and down to atomic dimensions and balance within a grain. Analogous to stress, strain can also be categorized into three types based on different length scales. In many cases, the macroscopic stresses and strains (Type I) have specific values under given applied load, while the magnitude of mesoscopic (Type II) and microscopic (Type III) stresses and strains may vary significantly through the body and be responsible for controlling the onset of failure. Consequently, investigating the stresses and strains at different scales, especially at the mesoscale and microscale, is crucial for understanding the performance of engineering components in service, as it allows the development of improved design methods for enhanced structural integrity.

The objective of the present research is to study the nature and the statistical distribution of the fluctuation of stresses and strains in polycrystalline alloys using different realizations of RVE with various microstructure. In this paper, a microstructurally flexible CPFE model was employed to simulate the mechanical properties of a polycrystalline alloy at the macro-, meso- and micro-scale. The model describes the macroscopic response to monotonic and cyclic loading for a range of RVE implementations. Material properties and grain orientations were assigned at integration points, with each grain contains dozens of integration points. The stress and strain magnitudes in each integration point were extracted, thus providing for the data for the quantification of microscopic deformation heterogeneity within grains. Additionally, via the use of finite element diffraction post-processing (FEDPP), the stress and strain field history were interpreted in terms of crystallographic orientation such that the mesoscopic properties (e.g. grain-orientation averages) could be extracted. The reproduced behaviour for average grain family elastic strains were then validated by matching the results of experimental neutron diffraction measurements.

## 2. Methodology

### 2.1. Rate-independent crystal plasticity formulation

The present model was implemented using the rate-independent constitutive equations following [Manonukul and Dunne \(2004\)](#). It was further modified and extended to account for elastic anisotropy, and to allow three-dimensional analysis for materials with various crystal structures ([Song et al., 2008](#)). [Dini et al. \(2006\)](#) introduced the diffraction post-processing interpretation to simulate the intragranular strains that can be directly comparable with the results of diffraction measurements.

The formulation is based on the multiplicative decomposition of the deformation gradient  $\mathbf{F}$  into elastic and plastic parts

$$\mathbf{F} = \mathbf{F}^E \mathbf{F}^P \quad (1)$$

The material undergoes plastic slip  $\gamma^\alpha$  on the slip system  $\alpha$ , through the undeformed crystal lattice, expressed as

$$\mathbf{F}^P = \mathbf{I} + (s^\alpha \mathbf{n}^{\alpha T}) \gamma^\alpha \quad (2)$$

Here  $\mathbf{I}$  is the identity tensor,  $s^\alpha$  and  $\mathbf{n}^\alpha$  are two mutually orthogonal vectors describing the slip direction and normal, respectively. The term  $\mathbf{F}^E$  represents elastic stretching and rigid-body rotations. The stress rate at arbitrary points within a grain during the deformation process is given by

$$\dot{\boldsymbol{\sigma}} = \mathbf{C} : \mathbf{D} - \boldsymbol{\sigma} \text{tr}(\mathbf{D}) - \boldsymbol{\Omega} \boldsymbol{\sigma} + \boldsymbol{\sigma} \boldsymbol{\Omega} - \sum_{\alpha=1}^N (\mathbf{C} : \mathbf{P}^\alpha + \beta^\alpha) \dot{\gamma}^\alpha \quad (3)$$

Here  $\mathbf{C}$  is the elastic moduli tensor,  $\beta^\alpha = \mathbf{W}^\alpha \boldsymbol{\sigma} - \boldsymbol{\sigma} \mathbf{W}^\alpha$ ,  $\mathbf{W}^\alpha$  being the skew part of the velocity gradient, and  $\mathbf{P}^\alpha$  the symmetric part of the velocity gradient.  $\mathbf{D}$  describes the deformation rate, and  $\boldsymbol{\Omega}$  denotes the spin tensor. All active slip systems will contribute to the overall plastic strain rate. The constitutive model uses a critical resolved shear stress,  $\tau_c^\alpha$ , as a state variable for the determination of plastic flow on each slip system  $\alpha$ . When the resolved shear stress on the  $\alpha$ th slip system,  $\tau^\alpha$ , exceeds the current critical resolved shear stress  $\tau_c^\alpha$ , that slip system is considered to become active. The critical resolved shear stress reflects the resistance of a slip system, and is allowed to evolve as a consequence of the current dislocation density and substructure. The yield surface has a polygonal shape in the stress space. The conditions under which a slip system is active are based on the yield and loading-unloading criteria. In order to calculate the Cauchy stress rate, the shearing rate  $\dot{\gamma}^\alpha$  on the  $\alpha$ th active slip system should be determined. The magnitude of  $\dot{\gamma}^\alpha$  can be determined using the constitutive equation for plastic slip on each slip system,

$$\dot{\tau}_c^\alpha = \sum_{\alpha=1}^N \mathbf{h}_{\alpha\beta} \dot{\gamma}^\alpha \quad (4)$$

Where  $\tau_c^\alpha$  is the current critical resolved shear stress. The hardening modulus  $\mathbf{h}_{\alpha\beta}$  represents the hardening on slip system  $\alpha$  due to shearing on slip system  $\beta$ . The rate of change of the resolved shear stress is given by

$$\dot{\tau}^\alpha = \mathbf{P}^\alpha : \left( \mathbf{C} : \mathbf{D} - \mathbf{C} : \sum_{\alpha=1}^N \mathbf{P}^\alpha \dot{\gamma}^\alpha - \boldsymbol{\sigma} \text{tr}(\mathbf{D}) \right) + \beta^\alpha : \left( \mathbf{D} - \sum_{\alpha=1}^N \mathbf{P}^\alpha \dot{\gamma}^\alpha \right) \quad (5)$$

To satisfy the consistency condition during plastic slip,

$$\dot{\tau}^\alpha = \dot{\tau}_c^\alpha \quad (6)$$

And hence, from [Eqs. \(4\) and \(5\)](#),

$$\sum_{\alpha=1}^N \mathbf{h}_{\alpha\beta} \dot{\gamma}^{\alpha} = \mathbf{P}^{\alpha} : \left( \mathbf{C} : \mathbf{D} - \mathbf{C} : \sum_{\alpha=1}^N \mathbf{P}^{\alpha} \dot{\gamma}^{\alpha} - \sigma \text{tr}(\mathbf{D}) \right) + \beta^{\alpha} : \left( \mathbf{D} - \sum_{\alpha=1}^N \mathbf{P}^{\alpha} \dot{\gamma}^{\alpha} \right) \quad (7)$$

Eq. (7) can be rewritten in the form

$$\sum_{\alpha=1}^N \mathbf{A}_{\alpha\beta} \dot{\gamma}^{\alpha} = \mathbf{b}^{\beta} \quad (8)$$

When the matrix  $\mathbf{A}_{\alpha\beta}$  is singular, the above equation has non-unique solutions. This problem can be overcome by using a singular-value decomposition to obtain a pseudo-inverse of the matrix  $\mathbf{A}_{\alpha\beta}$  (Manonukul and Dunne, 2004), and it is adopted here. The hardening modulus matrix can be simply described as

$$\mathbf{h}_{\alpha\beta} = [q + (1 - q)\delta_{\alpha\beta}]h. \quad (9)$$

Here  $h$  is the self-hardening rate and  $q$  denotes the latent-hardening ratio, with values in the range  $1 < q < 1.4$ . Hence, four material parameters need to be set in this model: the initial critical resolved shear stress  $\tau_c^{\alpha}$ , two hardening parameters, and the elastic moduli matrix.

## 2.2. Implementation of the CPFE model

There are mainly three types of RVE meshing homogenization methods for polycrystalline materials that are based on crystal plasticity theory: the voxel RVE model, truncated octahedron-based model and grain-based RVE model. The voxel model consists of cubic finite elements and each element corresponds to an individual grain. It is an efficient and effective way to model the collective behaviours of RVE, while this mesh method cannot be used to capture the grain shape or the heterogeneous intragranular deformation. The grain morphology in the truncated octahedron-based RVE model is more realistic represented than the voxel and grain-based model. Nevertheless, the required computation time of truncated octahedron-based RVE is much higher compared with the voxel and the grain-based model. Some research suggests that the detailed features of grain morphology has relatively small influence on the collective behaviours of RVE (Lim et al., 2019). Besides, the improvement of simulation accuracy achieved by octahedron-based RVE is not equivalent to the simulation time consumed (Abd El-Aty et al., 2018). Therefore, the grain-based RVE model is employed in current research. In the grain-based RVE model, each grain consists of many cubic elements, so it can effectively capture more details about grain morphologies and sizes distribution in polycrystalline materials. Such RVE model has been extensively used nowadays to investigate the grain scale tensile deformation (Abd El-Aty et al., 2018), fatigue indicator parameters (Stopka et al. 2020; Li et al., 2020) and texture evolution (Min et al., 2020) in different types of polycrystalline alloy.

Some published examples of RVEs used in the polycrystalline CPFE model, total numbers of grains and averaged number of elements with a single grain are listed in Table 1. According to the published data, 20-100 elements per grain is sufficient to perform grain level deformation analysis. Thus, for the purposes of the present study we select a grain-based RVE with  $30 \times 30 \times 30$  elements and 600 grains are accurate for the investigation of grain level stress and strain.

The crystal plasticity constitutive equations are implemented in the form of a user-defined material subroutine UMAT within the nonlinear finite element analysis package ABAQUS. Grain-based RVE models with periodic microstructure are generated using the DREAM.3D software (Groeber and Jackson, 2014). Lognormal grain size distribution and random grain orientation are used to construct the RVEs. Texture can be described by the choice of grain orientation distribution function (ODF). In this study, a set of RVE together with the assigned initial crystal orientations are referred to as a *microstructural realization*. It can be used to investigate statistical material response induced by a number of realizations once the deformation model is validated by one realization.  $30 \times 30 \times 30$  finite element meshes were introduced to the RVEs by using eight-node continuum elements (C3D8) of ABAQUS. The RVE used for validation contains 600 randomly oriented grains is shown in Fig. 1. The objective of this study was to use a simple but powerful numerical model to capture the multiscale nature of stress and strain distributions in polycrystalline materials. Each implementation of an advanced CPFE model for computational polycrystalline plasticity is predominantly considered as an instance for statistical purposes. However, the point-to-point and grain-to-grain variation contain rich information about real physical phenomena.

Some researchers have investigated the influence of crystal plasticity hardening framework on the deformation behaviour of polycrystalline materials. Lim et al. (2019) found that slip-based hardening constitutive equations can accurately reproduce the single

**Table 1**  
Examples of grain-based RVEs used in previous CPFE studies.

Material	Total numbers of grains	Total numbers of element	Average number of elements/grain	Refs.
Cu	125	8000	64	Moghaddam et al. (2017)
Ti-6Al-4V	263	13824	52	Stopka et al. (2020)
Al	1000	64000	64	Zhang et al. (2015)
Steel	151	12800	85	Alleman et al. (2018)
Al	3181	125000	39	Esmailpour et al. (2018)
Al	1000	27000	27	Zhang et al. (2019)



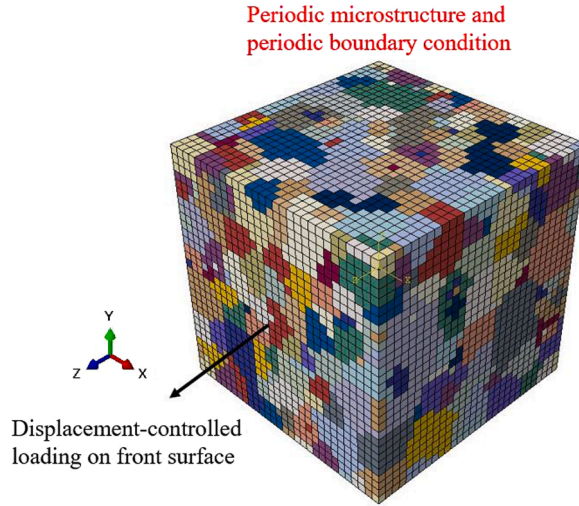


Fig. 1. The RVE model was subjected to periodic boundary conditions. Note: different colours represent different grains.

and polycrystal response of dislocation density-based hardening. Additionally, slip-based hardening law shows smaller relative error and smaller mesh sensitivity compared to dislocation density-based constitutive equations. Their finding provides firm basis for the selection of phenomenological constitutive equation (slip-based) hardening law in this research. To make the statistics results in this research widely applicable, a simple phenomenological constitutive equation is employed, and general conclusions are drawn.

Good results in terms of macroscopic (stress-strain curve) and mesoscopic (diffraction validation) response of materials can be achieved via using the grain-based RVE model with 600 grains. Fig. 1 illustrates the initial configuration of the RVE with periodic microstructure subjected to Periodic Boundary Conditions (PBC). In polycrystalline materials, the deformation of RVE can be non-uniform even if a uniform external loading is applied. It is well-known that PBC leads to smaller RVE sizes than a homogeneous boundary. PBC is implemented by coupling the displacements of the nodes of each pair of opposite faces of the RVE. Any over-constraint should be avoided when coupling nodes in eight vertices and twelve edges. The constraint equation is set by using the open-source ABAQUS plugin tool EasyPBC (Omairey et al. 2019). In this study, 8373 constraint equations are generated for the constructed RVE model. After setting the periodic boundary, displacement constraints are applied at RVE vertexes and a displacement-controlled loading is applied at the dummy node that constrains the relative displacement between the front and back surface in the third direction. The RVE has a cubic shape with a total volume of  $1 \times 1 \times 1 \text{ mm}^3$ . All the simulations were performed at room temperature.

### 2.3. Statistical distributions

Statistical analysis was carried out of the grain morphology and deformation characteristics of RVE polycrystalline assemblies. In this study, the spatial position of grains was randomly distributed, and the grain diameter was spatially non-correlated. Statistical distributions of size and stress-strain values during deformation were found to evolve towards continuous Gaussian (normal) and lognormal distributions.

The normal probability density function is given by

$$f(x|\mu, \sigma) = \frac{1}{\sigma\sqrt{2\pi}} \exp\left\{-\frac{(x - \mu)^2}{2\sigma^2}\right\} \quad (10)$$

where  $\mu$  and  $\sigma$  are the mean and standard deviation of the variable  $x$ , respectively.

The lognormal distribution is expressed by the function

$$f(x|M, S) = \frac{1}{xS\sqrt{2\pi}} \exp\left\{-\frac{(\ln x - M)^2}{2S^2}\right\} \quad (11)$$

where  $M$  and  $S$  are respectively the mean value and standard deviation of the variable  $\ln x$ .

## 3. Macroscopic response of RVE

### 3.1. The fitting of crystal plasticity model parameters

To calibrate the elastic and hardening parameters, the macroscopic response of RVE was first fitted to the monotonic stress-strain

curve for Haynes 282 alloy (a nickel-based superalloy). The crystal structure of this alloy is face-centred cubic (FCC), and it has 12  $\langle 1\bar{1}0 \rangle \{111\}$  slip systems. Fig. 2 shows the grain morphology and orientation within one RVE realization. A set of discrete grain orientations was generated to get random texture described by the Euler angles using Bunge's notation (shown in Fig. 2 (b)). The randomness of orientation can be further described by the multiples of random distribution (MRD) illustrated in Fig. 2 (c). The MRD value is the normalized probability density of a given orientation. It describes the factor by which specific orientations of crystallites are over-represented compared with the random condition. The higher number of MRD means a stronger texture, while a lower number represents a weaker texture. Under ideal conditions, an MRD value of 1 means perfectly random orientation. The values in Fig. 2 (c) are quite close to 1, indicating the set of orientations are randomly distributed and the grains are not textured. It is important to note that the same ODF is employed throughout the study.

Macroscopic stress and strain can be obtained from the overall response of the whole RVE. The material parameters that need to be fitted in this model are single-crystal elastic moduli, critical resolved shear stress and hardening parameters. In order to get a reliable evaluation of the above parameters, it is essential to reproduce both the macroscopic behaviours by fitting the macroscopic stress-strain curve and the mesoscopic property by matching the simulation result with neutron diffraction measurements. Optimal values of crystal stiffnesses can be determined by fitting the mesoscopic response of RVE obtained from finite element diffraction post-processing in the elastic region to neutron diffraction measurement of orientation-specific elastic strains. A detailed description of diffraction post-processing can be found in a later chapter. The macroscopic stress-strain curve can then be employed to evaluate the critical resolved shear stresses and hardening parameters. The macroscopic tensile stress-strain response obtained from the simulation is shown in Fig. 3, together with the experimental data (Jaladurgam et al., 2020). An excellent agreement has been achieved between CPFE reproduction and experimental observation. The corresponding elastic modulus matrix parameters, the critical resolved shear stress and hardening parameters are listed in Table 2. Here, we are interested in statistical analysis of the multiscale deformation behaviours of polycrystalline materials before failure occurs, especially when the loading point shows strong strain localization. Failures often originate from localized regions even when the macroscopic strain is small. When the global strain is 1.55%, the maximum plastic slip locally is  $\sim 6\text{--}7\%$  in our model. Finally, it should be noted that at the chosen total strain level the contributions from elastic and plastic are of approximately similar magnitude. This represents the most difficult condition for description compared to cases when either elastic or plastic deformations dominate.

### 3.2. The effect of crystal orientation permutation on the statistical variation of overall stress

In the first part of the present study, we focused our attention on the effect of *crystal orientation permutation*. We introduced this term to describe the variation of orientation assignment to grain seeds, and hence grains, without changing any of the individual grain shapes. The equivalent of this mathematical contrivance is not possible experimentally but is extremely useful in that it allows separating the influence of grain orientation from that of grain size and shape.

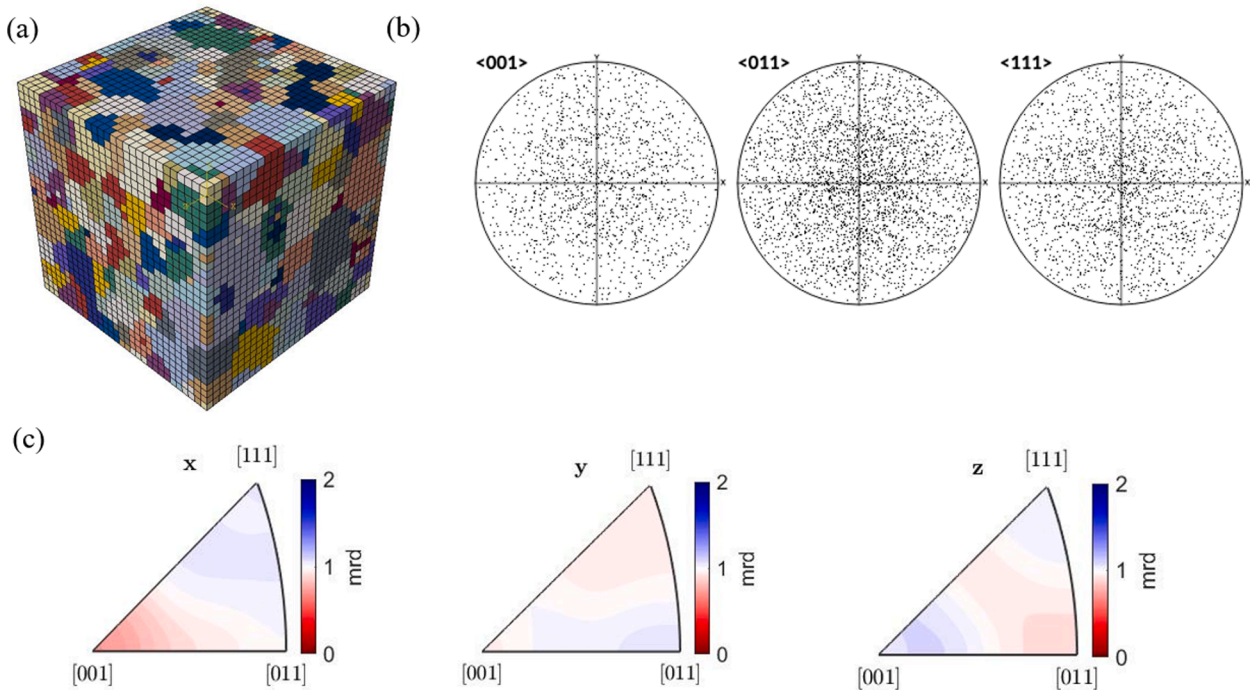


**Fig. 2.** The microstructure of RVE used for material parameters fitting. (a) microstructure (b) pole figures in three directions (c) multiples of random distribution for the used orientation.

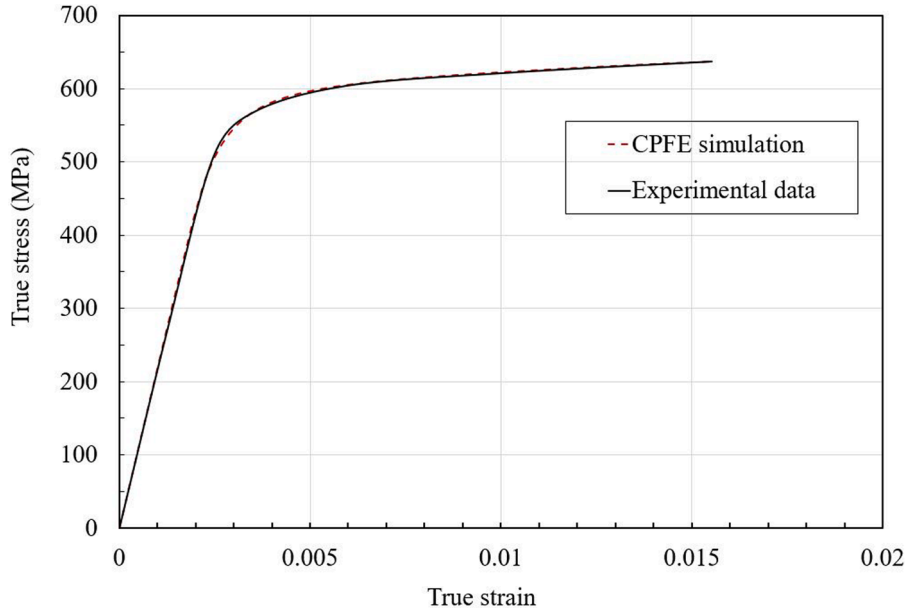


Fig. 3. Illustration of the macroscopic stress-strain curves under monotonic loading obtained from CPFE reproduction and experiment.

Table 2

Material parameters used in the simulation.

Stiffnesses (GPa)	CRSS (MPa)	$h$	$q$
C11 C12 C44			
250 160 118	257	$h = h_F[1 + (h_R - 1)\exp(-100h_{exp}\epsilon)]^*$	1.01

\*  $h_F = 950$ ,  $h_R = 14$ ,  $h_{exp} = 4$ .

The RVE model calibrated against experimental data was run with 48 realizations that used identical grain shapes, but randomly re-assigned orientations, to study the influence of orientation permutation on the material response statistics. In each of the 48 realizations, the grain morphologies are identical to each other, while the numbered list of crystal orientations is permuted randomly. Therefore, these realizations possess the same grain morphology and orientation distribution function, but correspond to different orientation permutations. In such a way, it is possible to eliminate the effect of grain morphology and to study the sensitivity of the mechanical response to one particular aspect i.e. crystal orientation.

The macroscopic stress-strain curves for all 48 realizations were obtained, and statistical analysis was performed to obtain the deviation between each curve and the average of them. The tensile loading was displacement-controlled, and all simulations were stopped when RVE reached 1.55% total strain. The overall stress  $\sigma_{1.55\%}$  in each realization was collected. Fig. 4 illustrates the averaged

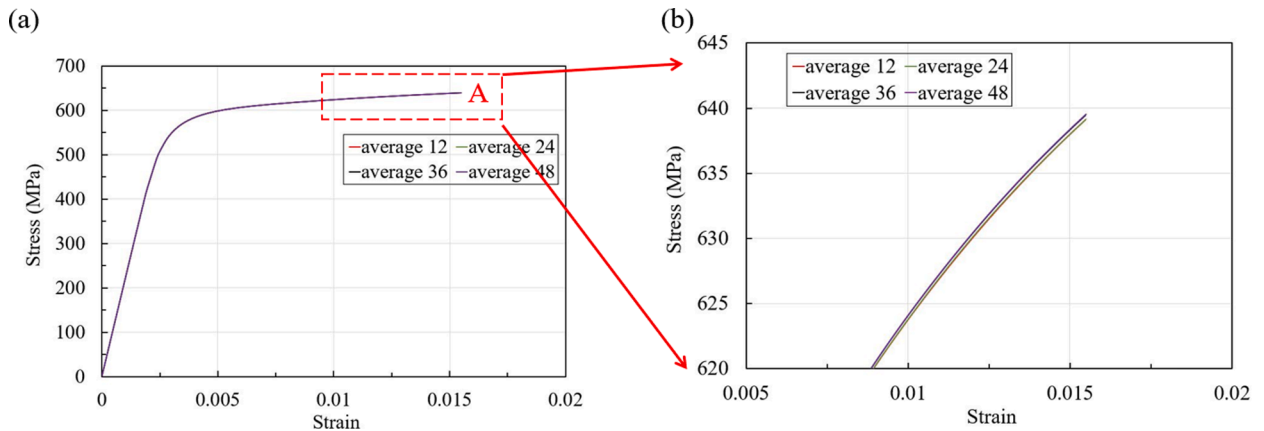


Fig. 4. (a) The averaged uniaxial stress-strain curves using 12, 24, 36 and 48 realizations. (b) An enlarged view of the rectangular area A.

stress-strain curves using a group of 12, 24, 36 and 48 realizations. As expected, the averaged curves gradually approach a certain ‘true’ average when the number of realizations increases, implying that the 3D cube considered is an effective RVE. The overall stresses in all realizations were averaged, and the difference from the mean value was calculated. As the dataset was too large to represent in one graph, the difference from the mean of 16 randomly chosen realizations is illustrated in Fig. 5. There is an apparent increase in scattering at the elastic-plastic transition region. The difference from mean first changes approximately linearly as the strain increases within the elastic region, and then shows a largely nonlinear relationship once the material begins to deform plastically. Analogous results could be obtained from the standard deviation of all 48 realizations. Once again, an apparent separation between the elastic and plastic regions can be recognised in the standard deviation curve depicted in Fig. 6.

To describe the statistics and to visualize the distribution of the simulation output, a histogram of overall stresses across 48 simulations was built and is shown in Fig. 7. Interestingly, the fluctuation of overall stresses at 1.55% total strain obtained from 48 simulations appears to follow a normal distribution. The Gaussian function fit to the histogram is shown by the continuous curve. The goodness of fit did not show significant improvement when the total number of realizations was increased above ~48. It was concluded that a further increase in the number of realizations was not warranted, as it would only raise the effort in terms of CPU time and hard drive space required without evident accuracy return. Despite some minor deviations between the fitting curve and points of the histogram, the fitting was reliable and allowed concluding that the overall stresses across all simulations follow a normal distribution.

The above finding leads to some challenging questions that deserve further study: Will the gaussian distribution remain the same for all realizations with different microstructures? What determines the width and height of the distribution? Up to now, only the effect of orientation permutation statistics was investigated. It is a well-known fact that the mechanical properties of polycrystalline alloys are tightly related to their microstructure that includes both grain morphologies and orientation. In the next section, more realizations will be considered and the influence of grain size and morphology on the variation of overall stresses will be studied.

### 3.3. The effect of grain morphologies on the fluctuation of overall stresses

A medium number of 600 grains was chosen in this part of the research. Seven more statistical ensembles with different grain morphologies were generated, each ensemble containing 48 realizations. The same numbered list of crystal orientations as used in the first set were used for the seven additional sets of realizations. Accordingly, the effect of grain orientation selection was moderated, and the mechanical response was compared between different ensembles. Table 3 lists the realization numbers with the assigned grain orientation and morphology. The microstructures of the eight ensembles with different grain morphologies are illustrated in Fig. 8. The grain size statistics of all ensembles obey the same lognormal probability density function as shown in Fig. 9. This particular distribution has been often reported in both experimental observations and simulations for grain size statistics in polycrystalline alloys (Quested and Greer, 2004; Berbenni et al., 2007a; Tucker et al., 2012; Xue et al., 2021). Thus, the morphology of each ensemble was nominally the same from a statistical point of view, but different locally.

Displacement-controlled uniaxial tensile loading was performed for all RVE ensembles to 1.55% total strain, and macroscopic stress data were collected. Fig. 10 (a–h) represents the histograms of the stress reached during deformation for ensembles with different grain morphologies, with Gaussian fitting applied to each. It is apparent that the distributions of overall stresses in the ensembles with eight grain morphologies were significantly different, although the mean value of stress for all ensembles was close to 639 MPa for all grain morphologies. Morphology 8 shows the widest stress distribution, while Morphology 3 presents the narrowest distribution. The macro-stress statistical distribution widths for other Morphologies fall in between those for Morphologies 3 and 8. The majority of macrostress values fall within the range 637 to 641 MPa indicated by the red arrows in Fig. 10 (j).

Since the same ODF was assigned to all sets of realizations, the variation of the overall stress distribution is affected by the dif-

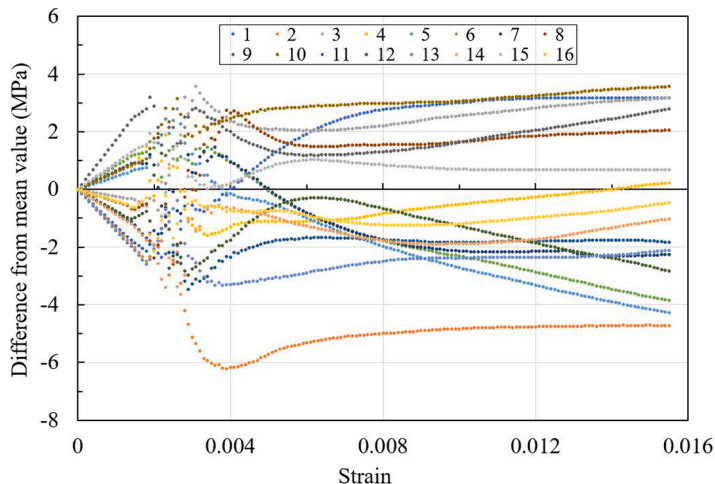


Fig. 5. The difference from the mean obtained from 16 realizations.

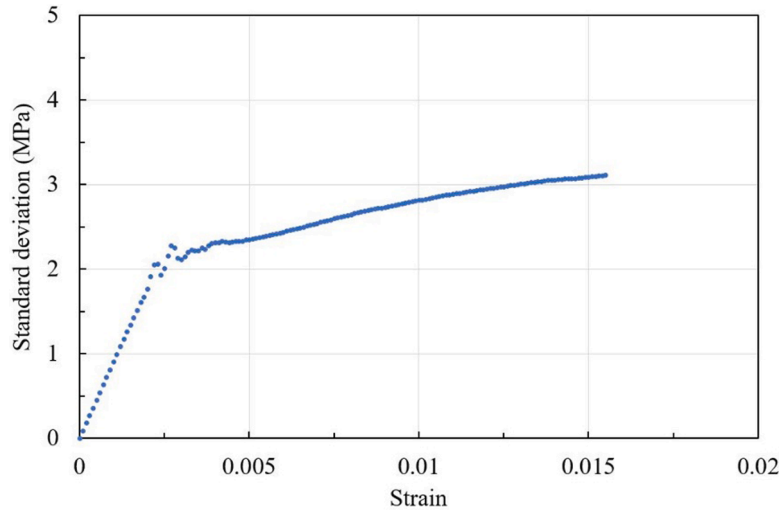


Fig. 6. The standard deviation of 48 realizations obtained during the loading process.

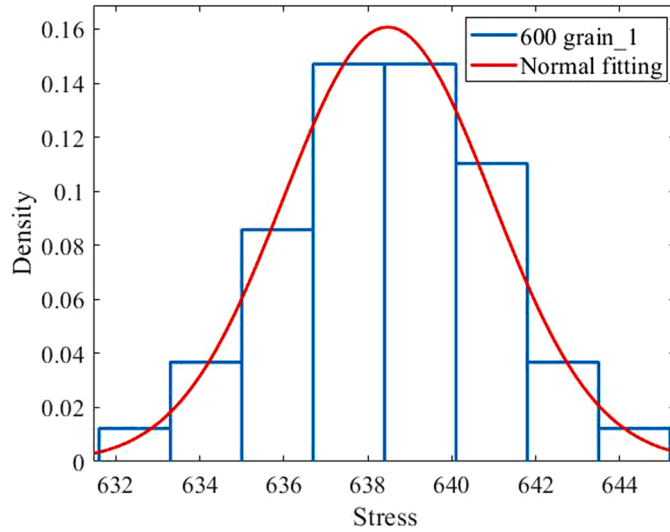


Fig. 7. Gaussian fitting to the histogram of overall stresses at 1.55% total strain across 48 realizations.

**Table 3**

Sets of realizations generated in this study.

Realization	No. of grains in RVE	Grain morphology	Average grain diameter ( $\mu\text{m}$ )	Grain orientation
1-48	600	1	147.1	Orientation permutation, same ODF
49-96	600	2	147.1	The same as corresponding realization 1-48
97-144	600	3	147.1	The same as corresponding realization 1-48
145-192	600	4	147.1	The same as corresponding realization 1-48
193-240	600	5	147.1	The same as corresponding realization 1-48
241-288	600	6	147.1	The same as corresponding realization 1-48
289-336	600	7	147.1	The same as corresponding realization 1-48
337-384	600	8	147.1	The same as corresponding realization 1-48
385-432	22		442.8	Orientation permutation, same ODF
433-480	99		268.2	Orientation permutation, same ODF
481-528	345		176.9	Orientation permutation, same ODF
529-576	1208		116.5	Orientation permutation, same ODF
577-624	2005		98.4	Orientation permutation, same ODF



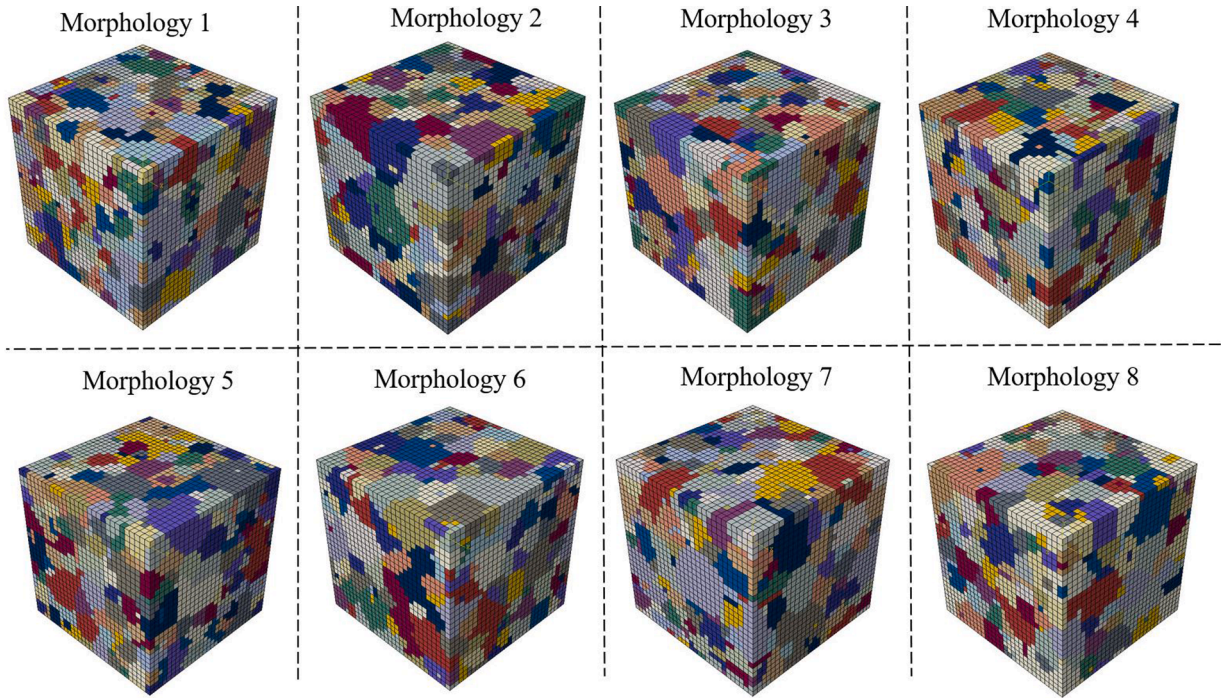


Fig. 8. An illustration of the microstructure of the eight ensembles with distinct grain morphologies.

ference in the grain morphologies, or, more specifically by the combination of grain shape and orientation. Although the eight sets of grain morphologies were generated by the same algorithm and parameters, since only a finite number (600) grains was generated, some difference was present among various realizations in terms of the *discrete* distribution of grain size. The fitting parameters for overall stress normal distribution and grain size lognormal distribution in different sets of realizations are listed in Table 4. In the current study, we found that not only the mean grain size plays a role but also grain size dispersion has an impact on the overall yield stress and hardening behaviour in this simple yet powerful phenomenological crystal plasticity model. In view of the fact that the discrepancy of grain size distribution is minor among different morphologies in the current study, it seems problematic to obtain a quantitative description of the correlation. Yet the overall trend of the correlation can be confidently determined as there is an apparent correlation between the standard distribution of average stress in an ensemble of RVEs with the grain size distribution in the RVE. It is interesting to find that the morphology with a larger grain size dispersion (larger  $S$ ) will result in fewer overall stress discrepancies (smaller  $\sigma$ ). This finding is consistent with previous simulation results in the literature (Berbenni et al., 2007b). As opposed to grain Morphology 8, Morphology 3 has a widely dispersive grain size distribution and corresponds to the narrowest overall stress distribution. The correlation between the grain size distribution parameter (standard deviation  $S$ ) and the overall stress distribution parameter (standard deviation  $\sigma$ ) is illustrated in Fig. 11. The physical explanation of the phenomenon highlighted here is that broad grain size dispersions tend to reduce the grain size dependence whereas the individual grain behaviour is grain-size dependent according to the discretization induced size effect addressed in the following section.

### 3.4. The effect of grain sizes on the fluctuation of overall stresses

To quantify the influence of grain size on the overall effective response, six more statistical ensembles (sets of realizations) with different mean grain sizes (grain numbers) were generated, each ensemble contains 48 realizations. The same random ODF was used for all ensembles and the realizations in each ensemble have different grain orientation permutations. Accordingly, the effect of grain orientation selection was moderated, and the mechanical response was compared between different ensembles.

As illustrated in Fig. 12, each ensemble contains different grain numbers, i.e., 22, 99, 345, 600, 1208 and 2005 grains. Each RVE has the same volume, therefore, RVEs with larger grain numbers correspond to smaller average grain sizes. The grain size within an RVE follows a lognormal distribution. The overall stress is the maximum stress value when loading is stopped. The magnitude of overall macroscopic stress  $\sigma_{1.55\%}$  and the yield stress  $\sigma_{0.2\%}$  in each realization were collected when the total strain reached 1.55%. Figs. 13 and 14 show that the distribution of  $\sigma_{1.55\%}$  in each ensemble follows a normal distribution. The width of the distribution decrease with increased grain number. In engineering design, components with a narrower property discrepancy are expected to be more reliable for the purposes of structural integrity. This study shows that the RVE with a larger number grain is more reliable in the statistical respect.

As shown in Fig. 15, the mean of the stress distribution increases with increasing grain number, indicating that smaller grain size strengthens this polycrystal alloy. The average yield stress  $\sigma_{0.2\%}$  and the flow stresses  $\sigma_{1.55\%}$  against the reciprocal square root of the grain size are plotted in Fig. 16. Straight trendlines are fitted by the least square method. Please note that both the error bars and



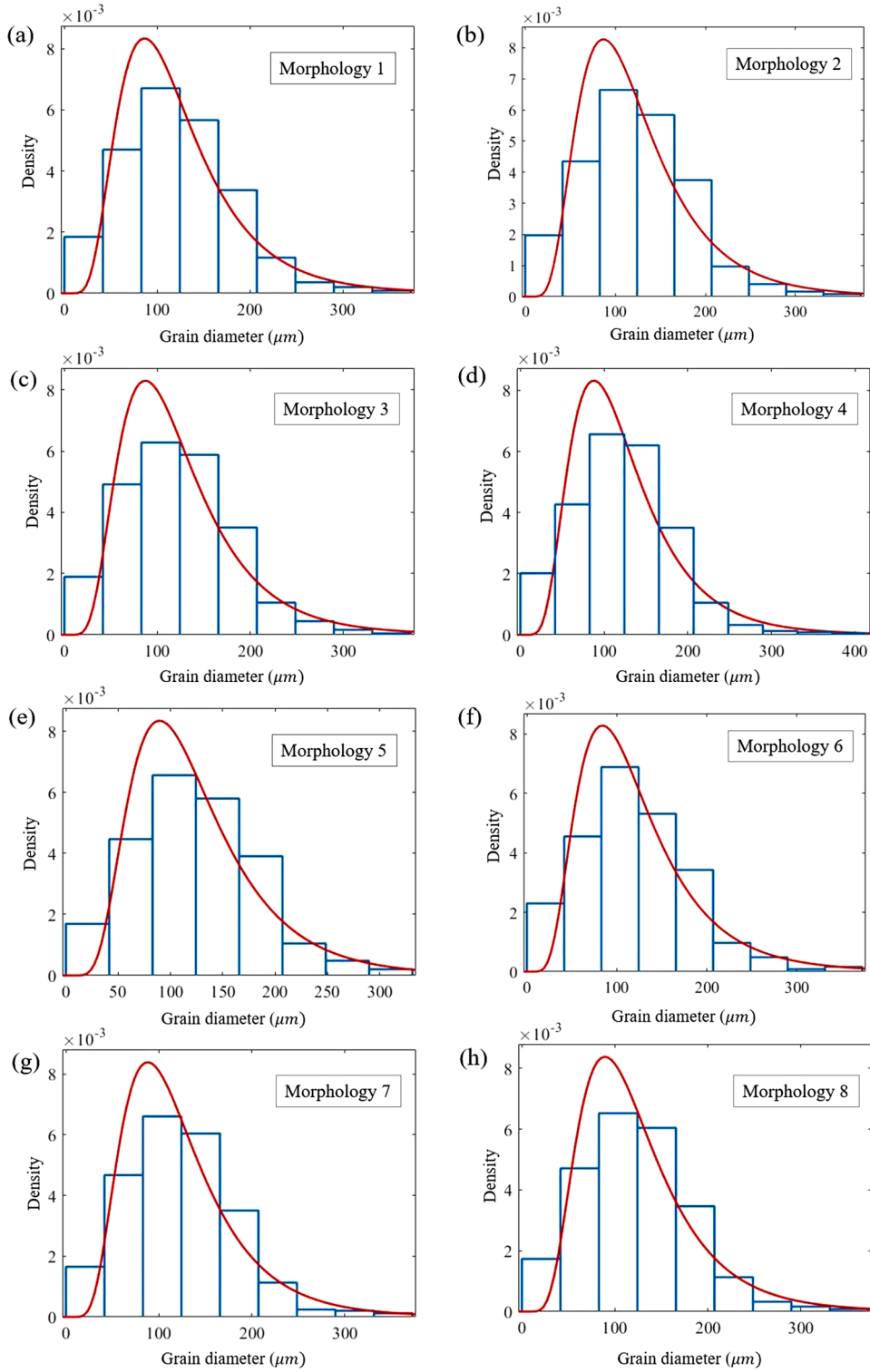
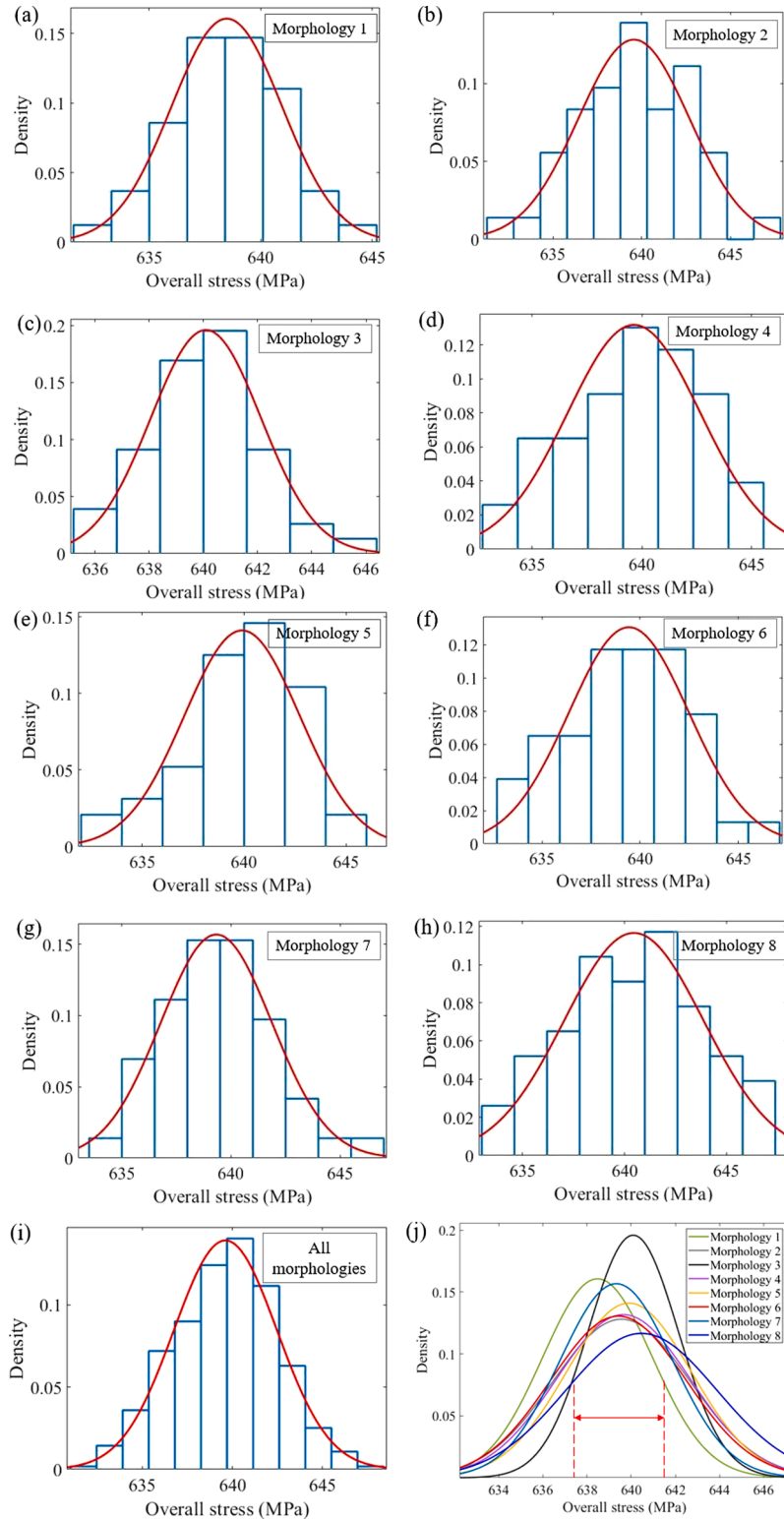


Fig. 9. (a–h) The grain size distribution fitted by a single common lognormal distribution for different grain morphologies.

confidence intervals are very small because of the excellent fitting of the data. Since internal length scales are not considered in the constitutive formulation, they remain the same simulations and there is no Hall-Petch relationship. The Hall-Petch like correlation in Fig. 16 might come from discretization and statistics induced size effect or one of them. Some researchers suggest that long-range *intragranular* correlations will induce a slower decay of the fluctuations of strain and stress (Kapetanou et al., 2015). We are here

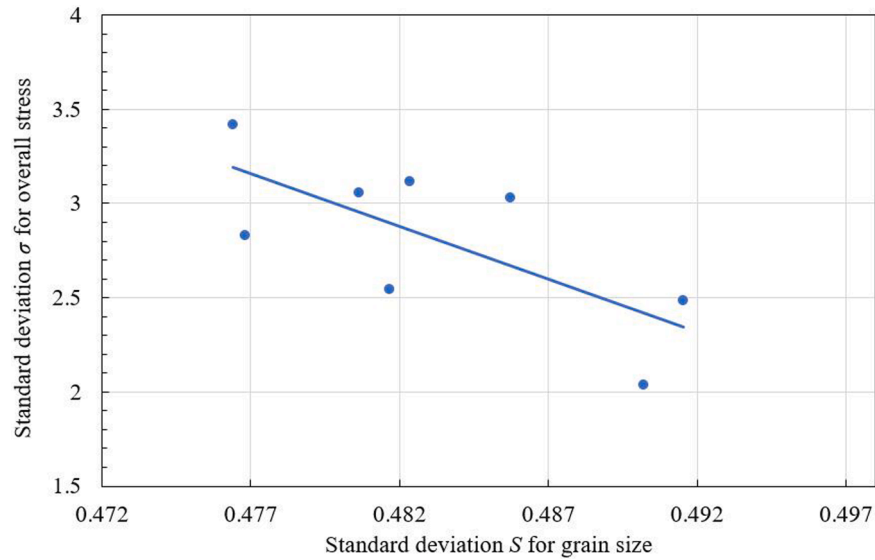
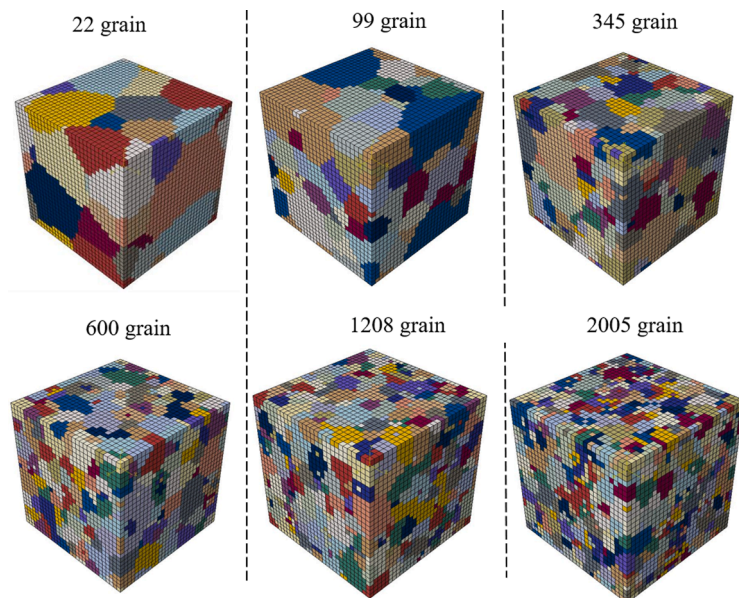


**Fig. 10.** Histograms and Gaussian fitting of overall stresses obtained from each set of morphology (a–h) and all morphologies (i). (j) Probability density of macroscopic stress distribution for eight sets of realizations.

**Table 4**

Normal fitting parameters of the overall stress and lognormal fitting parameters of grain size distribution.

Morphology	Grain size fitting parameters		Overall stress fitting parameters	
	$M$	$S$	$\mu$	$\sigma$
1	4.699	0.492	638.476	2.482
2	4.706	0.482	639.561	3.115
3	4.706	0.490	640.090	2.035
4	4.710	0.486	639.646	3.027
5	4.721	0.477	639.898	2.828
6	4.685	0.481	639.420	3.054
7	4.709	0.482	639.327	2.544
8	4.718	0.476	640.462	3.420

**Fig. 11.** A correlation between lognormal grain size distribution fitting parameter  $S$  and normal overall stress distribution fitting parameter  $\sigma$ .**Fig. 12.** RVE realizations with different grain sizes in which different colours indicate different grains.

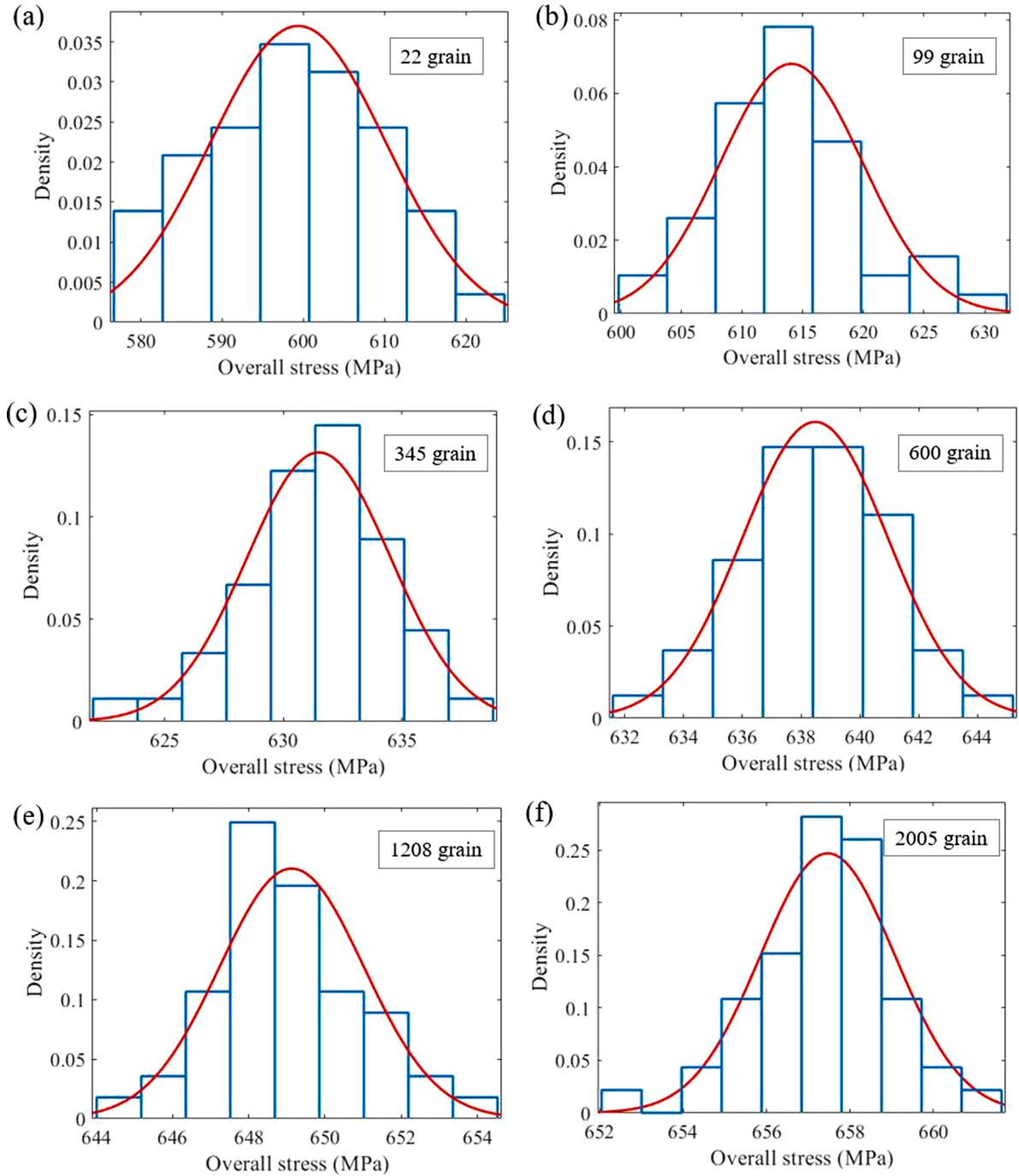


Fig. 13. Histograms and Gaussian fitting of overall stresses  $\sigma_{1.55\%}$  obtained from each ensemble with different mean grain sizes.

mainly focusing on the long-range *intergranular* correlations of size effect and no decay was shown in our research.

### 3.5. Discretization and statistical induced size effect

The size effect in the current study can be classified as discretization induced size effect and statistical induced size effect. The former is caused by the discretization of grain (the number of elements per grain), while the latter statistical effect arises from different numbers of grains in the RVE. It is important to separate these two effects when performing a systematic study of the size scaling of stress fluctuations. If the grain size, RVE size and element size are changed proportionally, the simulation results will be the same as the

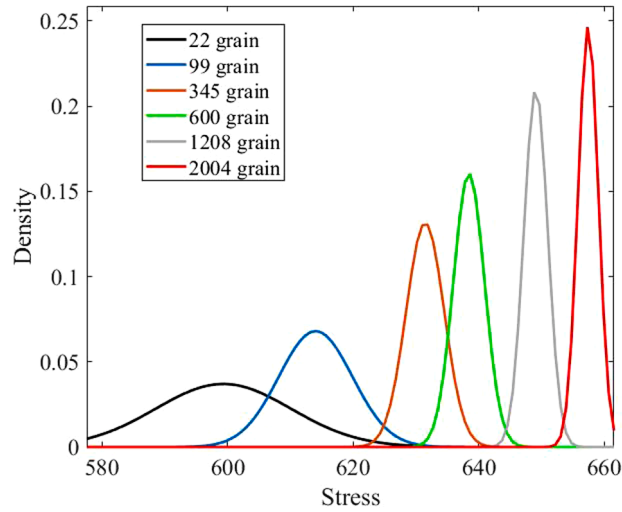


Fig. 14. Probability density of macroscopic stress  $\sigma_{1.55\%}$  distribution for six sets of realizations

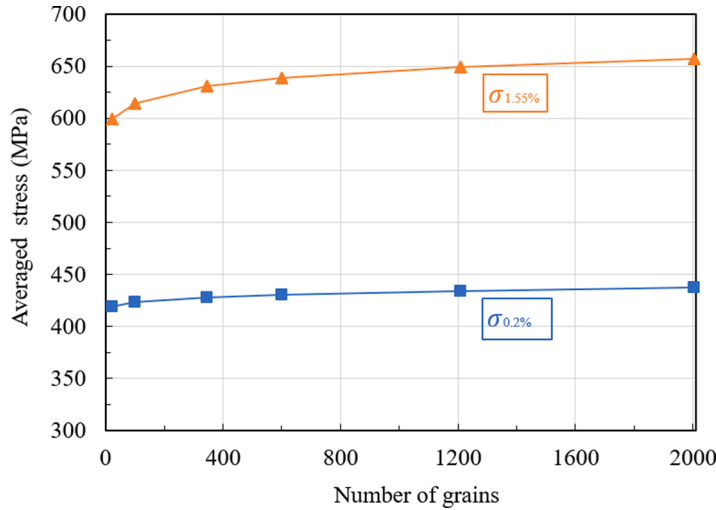


Fig. 15. Comparison of the averaged overall stress in each ensemble when total strain equals 0.2% and 1.55% versus the number of grains.

original configuration. The above statement provides the foundation for the following study of size fluctuation.

To evaluate the discretization induced size effect, four more RVE ensembles with different mesh discretization (as shown in Fig. 17) were generated, each ensemble contains 10 realizations. RVEs in each ensemble have 600 grains and the same element size, while the grain size and RVE size were increased proportionally. The grain microstructure was changed proportionally compared to the corresponding RVE in other ensembles. In this case, the number of grains in the RVE is fixed, it will not have a statistical induced size effect. But the number of elements per grain increases, hence only the discretization induced size effect will be investigated. Table 5 summarizes these RVE parameters.

The average yield stress  $\sigma_{0.2\%}$  and the flow stresses  $\sigma_{0.3\%}$ ,  $\sigma_{1.55\%}$  obtained from these four ensembles against the reciprocal square root of the grain size are plotted in Fig. 18. It is interesting to find that discretization effect will introduce a Hall-Petch like relationship in polycrystalline materials. Since internal length scales are not considered in the constitutive law, it is not a real Hall-Petch relationship but is only called Hall-Petch like behaviour. Here we demonstrate that discretization can lead to a Hall-Petch like relationship when the number of elements per grain ranges from 1.2 to 45 on average per RVE. To the best of the author's knowledge, no known relevant literature regarding discretization and Hall-Petch like relationship has been published yet.

To quantify the statistical induced effect on the overall effective response, four ensembles with fixed RVE size (as shown in Fig. 19) were generated, each ensemble contains 48 realizations. Again, the same random ODF was used for all ensembles and the realizations in each ensemble have different grain orientation permutations. RVEs in each ensemble have a volume of  $1\text{mm}^3$ , while the grain size and the element size were changed proportionally to keep the same number of elements per grain among different RVE ensembles. Therefore, discretization effects on the grain scale that arise from the pixelation of the grain morphologies by the cubic elements do

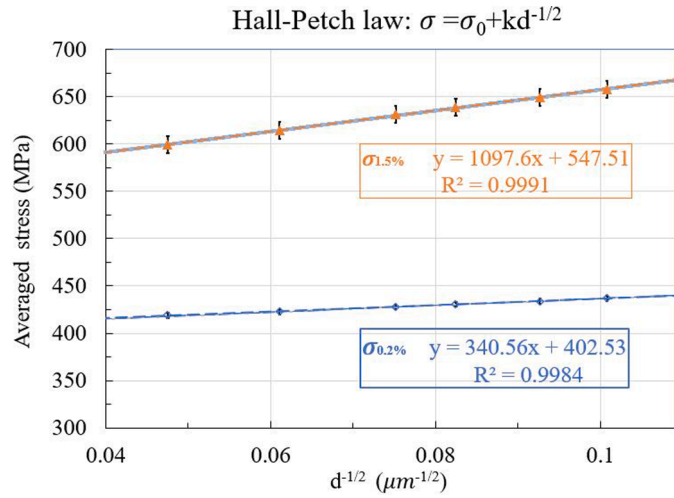


Fig. 16. Illustration of the Hall-Petch like relationship captured by the simulation.

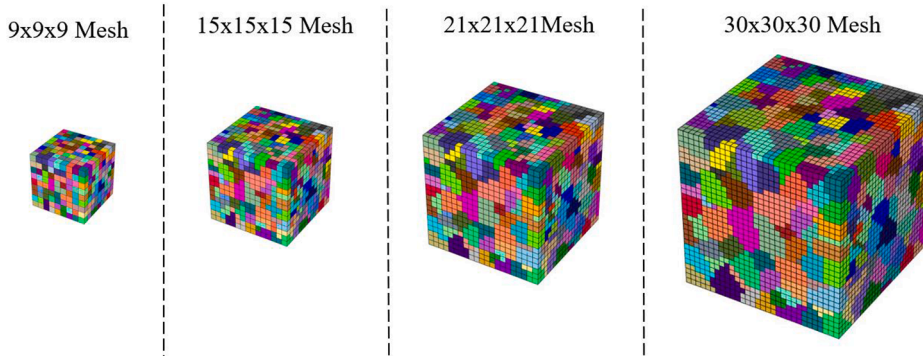


Fig. 17. RVE realizations with different mesh discretization in which different colours indicate different grains.

Table 5

RVE size, grain numbers and mesh variation parameters.

Realization	No. of grains in RVE	RVE volume ( $\mu m^3$ )	Total numbers of element	Average number of elements/grain
625-634	600	$300^3$	$9^3$	1
635-644	600	$500^3$	$15^3$	6
645-654	600	$700^3$	$21^3$	15
655-664	600	$1000^3$	$30^3$	45
665-712	22	$1000^3$	$10^3$	45
713-760	75	$1000^3$	$15^3$	45
761-808	178	$1000^3$	$20^3$	45
809-856	600	$1000^3$	$30^3$	45

not change, and only the statistical induced size effect was studied.

As illustrated in Fig. 20, the distribution of  $\sigma_{1.55\%}$  in each ensemble follows a normal distribution. The mean of a normal distribution is not observed to obey any particular correlation with the number of grains in the RVE, while the standard deviation of the distribution decreases significantly with increased numbers of grains as shown in Fig. 21. Since there is no observed statistical induced size effect in this research, it is then reasonable to conclude that the Hall-Petch like behaviour reported in Section 3.4 arises from the discretization induced size effect. This study also suggests that RVEs with more grains are preferred for engineering design in the statistical respect.

#### 4. The mesoscopic response of RVE

One of the main challenges of CPFE model validation arises from the fact that the uniaxial stress-strain curves only provide an incomplete description of plastic flow as they reduce a six-dimensional yield surface to the one-dimensional yield curve. It means that



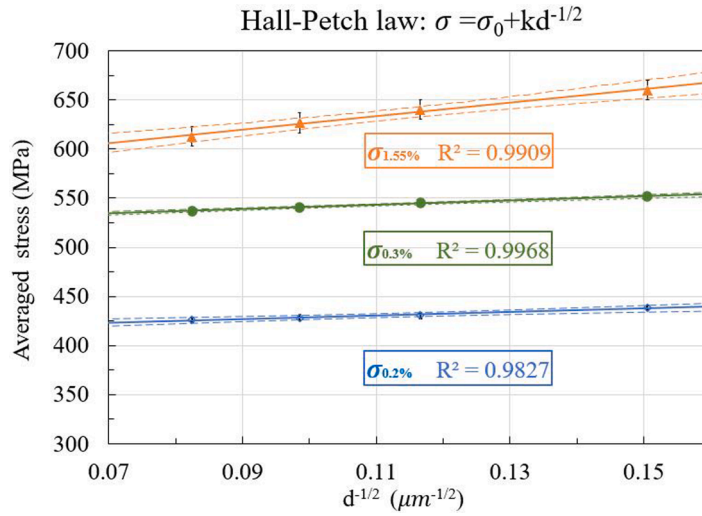


Fig. 18. Illustration of the discretization induced size effect (Hall-Petch like effect).

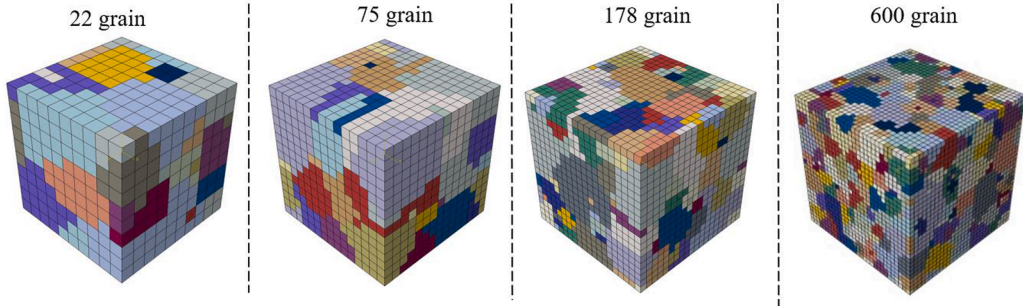


Fig. 19. RVE realizations with different grain numbers and element sizes.

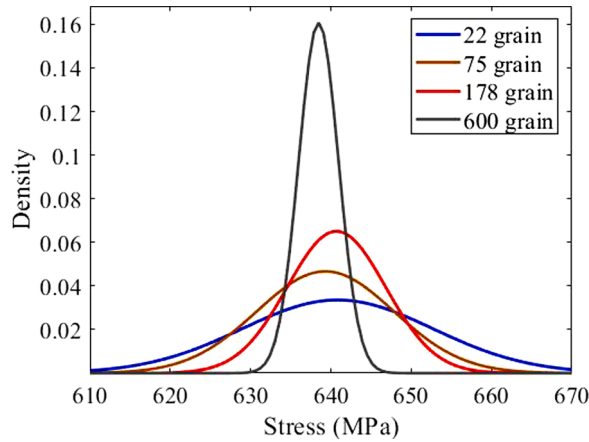


Fig. 20. Probability density of macroscopic stress  $\sigma_{1.55\%}$  distribution for four sets of realizations.

acceptable agreement with monotonic stress-strain curve can be obtained using different combinations of material parameters, such as single-crystal elastic moduli, critical resolved shear stress, hardening parameters, etc. In order to get a reliable evaluation of the above parameters, it is essential to reproduce both the macroscopic and mesoscopic behaviours of RVE and fit the result with experimental measurements. With the help of diffraction post-processing, optimal values of crystal stiffnesses can be determined by fitting the mesoscopic response of RVE obtained from different grain groups in the elastic regime to diffraction measurement of orientation-

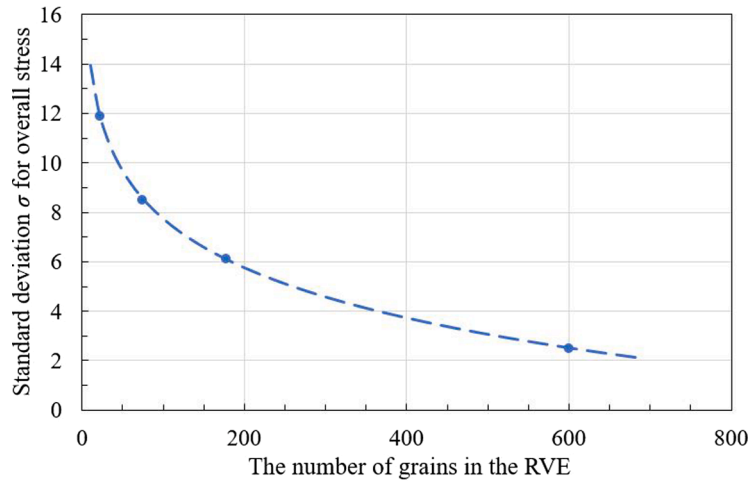


Fig. 21. An illustration showing the decreased standard deviation for overall stress with an increased number of grains in the RVE.

dependent elastic strains. The post-yielding behaviour can then be employed to evaluate the critical resolved shear stresses and hardening parameters.

The optimal material parameters for mesoscale fitting are listed in Table 2, and the simulation results from diffraction post-processing are depicted in Fig. 22, together with the neutron diffraction data of Haynes 282 alloy (Jaladurgam et al., 2020). Jaladurgam et al. employed *in-situ* neutron diffraction experiments to evaluate the elastic lattice strains in different reflection groups. The result for Haynes 282 alloy with coarse gramme prime in their research was used to validate our model. The error bar in Fig. 22 is from experiment data. Good agreement has been achieved, considering the fact that a relatively small number of grains (600) were used in this model. This model can well reproduce the anisotropic elastic-plastic behaviour for all grain groups, especially for the 111, 220 and 311 families, and somewhat less precisely for the 200 grain family. Considering the goodness of fitting shown in Figs. 3 and 22, it is suggested that both macroscopic and mesoscopic behaviour of elastic strains are adequately captured by the current model.

## 5. The microscopic response of RVE

In Section 3, the macroscopic stresses under monotonic loading obtained from multiple realizations were found to follow a normal distribution. The macroscopic overall stresses of the RVEs are relatively stable, lying within a 2% difference band for the eight grain morphology ensembles used. It is important to note, however, that failure is governed by local stress and strain values that may show a greater degree of variation. It is therefore interesting to directly investigate the distribution of local stresses and strains within RVEs. For each realization, approximately 300000 IPs are used in one RVE with 600 grains, suggesting that each grain contained around 500

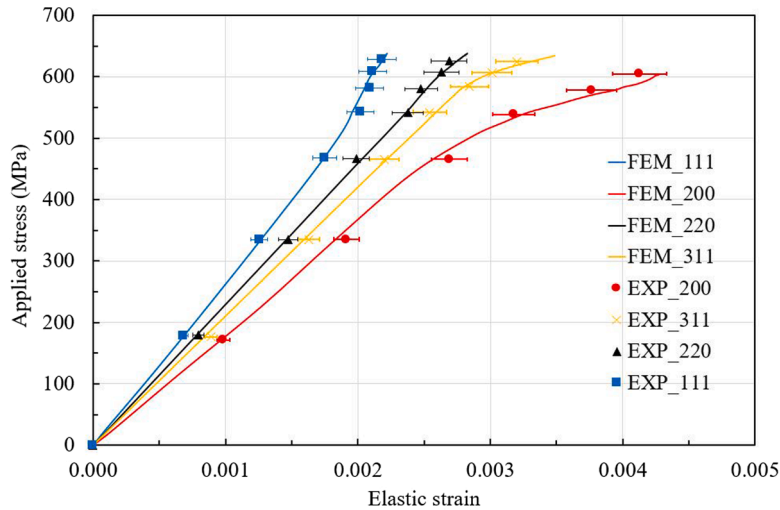


Fig. 22. Comparison between CPFE diffraction post-processing reproduction and experimental diffraction data for Haynes 282 under monotonic loading.

IPs on average. Diard et al. (2005) examined the relationship between IP numbers and grain numbers that are sufficient for adequate deformation description. According to their results, it is found that 25 IPs per grain could be sufficient to provide an adequate reproduction in the case of small deformation. It should be pointed out that a detailed representation of intragranular stresses and strains were not attempted in the current study. The aim is to develop a computationally efficient model that captures the macro-meso-microscopic behaviour of RVE and to analyse the model reproduction statistically.

As the loading was applied in the  $z$  direction, the local stress, elastic and plastic strain components of interest are termed  $\sigma_{zz}$ ,  $\epsilon_{zz}^{el}$  and  $\epsilon_{zz}^{pl}$ , respectively. At each integration point, the local stress and strain values can be readily collected. After total strain reaches 1.55%, the distributions of stresses and strains at IPs were examined for several realizations. They were found to show the same type of distribution, therefore the results from only one randomly selected realization are illustrated here in Fig. 23. In Fig. 23 (a), it is evident that local stress  $\sigma_{zz}$  follows a normal distribution, and the range of fluctuation is as large as  $639 \pm 400$  MPa. In contrast, the histogram in Fig. 7 shows that the overall macroscopic stresses at the chosen strain level (1.55%) across 48 realizations follow a much narrower normal distribution within  $639 \pm 6$  MPa. It is worth mentioning that stress is directly related to elastic strain through generalised Hooke's law, implying the distribution of local elastic strain should also have a normal profile, as illustrated in Fig. 23 (b). The local plastic strain distribution is observed to follow a lognormal distribution, as shown in Fig. 23 (c). The lognormal profile shape suggests that plastic strain accumulation is a multiplicative process, and it does not increase uniformly as deformation proceeds – it becomes progressively localized and the local regions of large strains make a significant contribution to the overall average strain increase. When the total deformation is large, the plastic strain becomes dominant, and hence the total strain appears to follow a lognormal distribution that has been reported in the literature (Tang et al., 2020). The overall strain of the whole RVE reaches precisely 1.55%, whereas the value of local elastic and plastic strain vary significantly within the RVE. The above finding is statistically significant, as it represents the fact that the variation of microscopic response is much broader than the macroscopic average. More importantly, local elastic strain, as well as stress, were found to obey a normal distribution, whereas the statistics of local plastic strain conforms to a lognormal distribution. The results reveal the nature of strain inhomogeneity at the microscale and emphasize the fact that the elastic

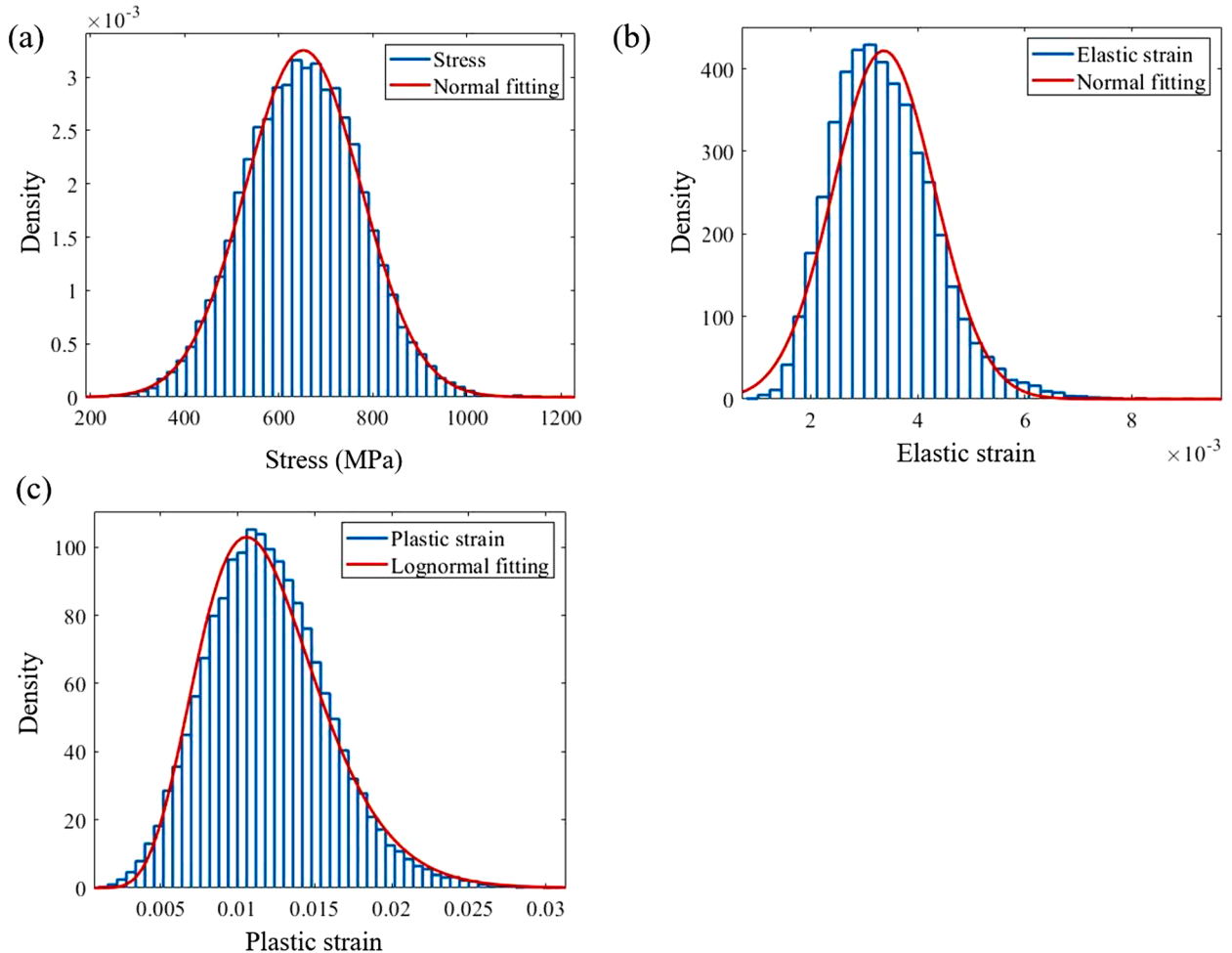


Fig. 23. The distribution and fitting of local  $\sigma_{zz}$  (a),  $\epsilon_{zz}^{el}$  (b) and  $\epsilon_{zz}^{pl}$  (c) across all IPs in one randomly selected realization.

strain accumulation represents an additive process, whereas plastic deformation is a multiplicative process. For the causes of this phenomenon, readers can refer to our previous publication (Chen and Korsunsky, 2021).

Equiaxed grains were employed in all the realization in the current study. It is also found that the fitting for normal and lognormal distribution will be more accurate when the RVE contains sufficient grains (at least  $\sim 200$  grains) and enough small mesh sizes (at least  $8 \times 8 \times 8$ ). It is then reasonable to assume that the statistic results of local stress and strain are convincing based on sufficient equiaxed grains and small mesh sizes. Nevertheless, it is believed that our finding has significantly broader applicability for grain morphologies. Fig. 24 (a) illustrates an RVE with a rolled grain morphology. The averaged long semi-axis of the equivalent ellipsoid is 10 times larger than the averaged short semi-axis. Uniaxial loading was applied to the RVE and the loading is stopped when the magnitude of total strain reached 1.55%. Analogous to the results obtained from equiaxed grains, the normal and lognormal strain distribution assumption appears to remain valid for RVEs with a rolled grain morphology, as shown in Fig. 24 (b) and (c).

Our previous examination indicates that our statistic results of local stress and strain are convincing when global strain ranges from 0–10% (Chen and Korsunsky, 2021). Significant strain localization occurs when the global strain is above 5% and corresponds to the long ‘tail’ in the lognormal strain distribution. Fig. 25 depicts the local elastic and plastic distribution when the total strain is 20% and 30%. Further investigation suggests that the distributions of local elastic and plastic strain obtained from the current model can still be described by normal and lognormal distributions to some extent even when the global strain is larger than 20%. However, the fitting quality for strains larger than 20% is not as good as that for smaller strains less than 10%, especially in the case of elastic strain and normal distribution. Such behaviours can be explained by the fact that a *small strain kinematic formulation* was implemented in the current study and the crystal orientations remain static throughout the FEM calculation. Grain rotation will be significant when investigating large deformation. As discussed in the previous section, large deformation that more than 20% lies beyond the scope of our current paper. A global strain of 1.55% was chosen because it represents the most difficult condition for description compared to cases when either elastic or plastic deformations dominate.

The normal elastic strain and lognormal plastic strain distribution laws are conditional upon the macroscopic homogeneity of deformation within the volume of interest. A large deviation can be expected to be observed when investigating the statistical distribution of strains and stresses within individual grains. The dislocation introduced stress/strain fields were studied by (Groma and Bako, 1998), and Kapetanou et al. (2015) on the level of dislocation simulations. (Groma and Bako, 1998) found the stress field generated by the dislocations can be approximated as the sum of a stochastic and a slowly varying component. However, their model only had a few hundred of parallel edge dislocations and the volume of interest is nanoscale. They mainly focus on the probability distribution of shear stress, not the strain and stress in the loading direction as in our research. Kapetanou et al. (2015) employed a 3D

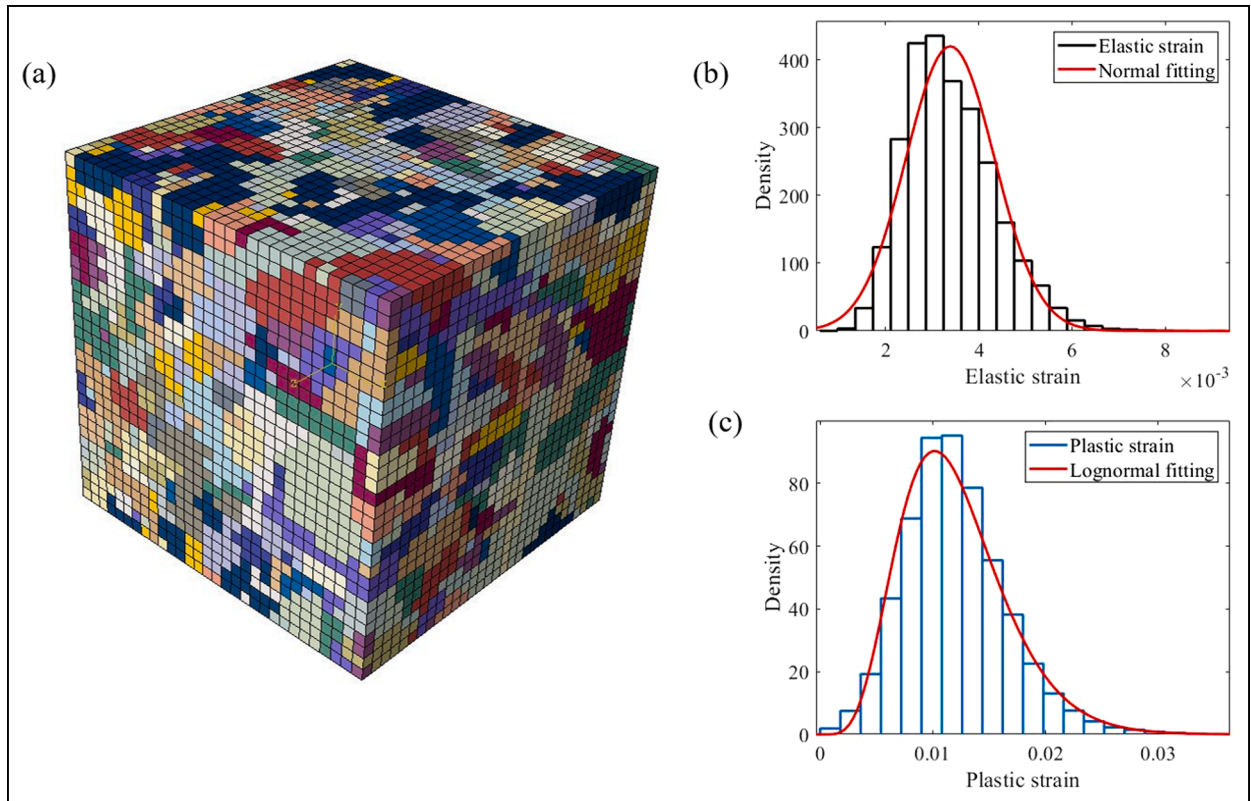


**Fig. 24.** (a) an RVE model with a rolled grain morphology. (b, c) normal and lognormal fitting for elastic and plastic strain, respectively, when the total strain reached 1.55%.

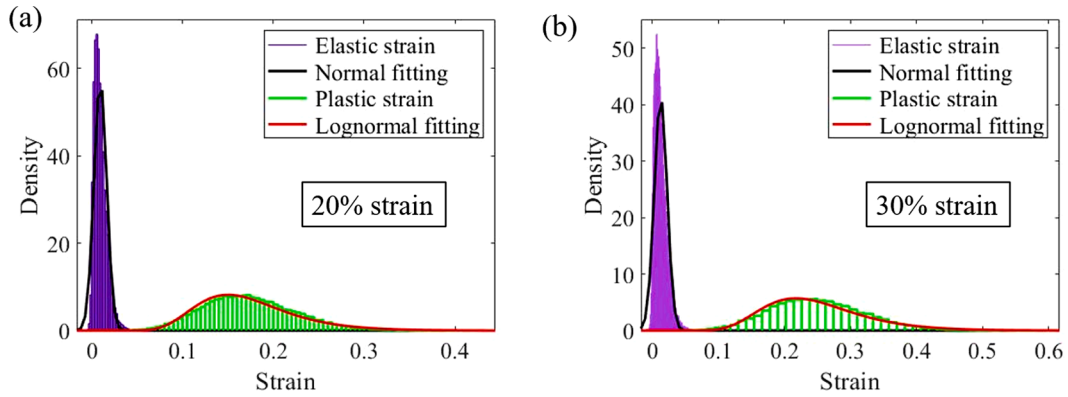


Fig. 25. The distribution of local elastic and plastic strain when the total strain reached 20% and 30%.

discrete dislocation model with a volume of only  $3\mu\text{m}^3$  and their simulation suggests that the fluctuations of strain and stress decay are in inverse proportion with the increase of the averaging volume, which is consistent with our simulation results that the fluctuation of smaller scale local stress ( $639 \pm 400$  MPa) is much larger than overall macroscopic average stresses at the chosen strain level (1.55%) across 48 RVE realizations ( $639 \pm 6$  MPa). Fig. 26 depicts the probability density distribution of elastic and plastic strains within 6 large grains, each containing a large number of 1000–1500 IPs. Due to the low number of values in each data set, the quality of discrete statistical distribution is moderate. Nevertheless, the normal and lognormal strain distribution assumptions remain valid for grains 1, 3, 4 and 6. However, for the other grains, the elastic and plastic strain statistics do not follow a distinct distribution. It is interesting to find that if the elastic strain in one grain conforms to a normal distribution, then the plastic strain obeys a lognormal distribution in the same grain. We speculate that these two particular types of statistical distribution are coupled within the same volume of interest. Table 6 lists the grain number and its corresponding reflection group with respect to the loading direction. According to the diffraction postprocessing data illustrated in Fig. 22, the 220, 311, 331 and 531 planes show higher linearity compared to 111 and 200 planes. Strain heterogeneities increase when local behaviour becomes strongly non-linear. In this research, we state that local elastic strain (stress) and plastic strain universally within the whole RVE follow a normal distribution and lognormal probability distribution, respectively. It is not expected nor claimed that the local elastic and plastic strains within *each* grain follow these particular distributions. Further investigation suggests that 233 out of 600 grains show this kind of distribution characterization. Among these 233 grains, 99 out of 102 grains are from 220, 311, 331 and 531 related reflection groups. It is therefore hypothesized that the strains within grains (Type III or microscale) that belongs to the high linearity reflection group (Type II or mesoscale) will show normal or lognormal distribution characterization.

Local stress and strain deviation from the macroscopic average (Type I) can be further classified into Type II (grain level) and Type III (intragranular deviation from grain average) that is highly inhomogeneous due to the difference in crystal orientation and intra-grain strain localization due to plastic slip. We notice that stresses within polycrystals are multi-scale, and the separation of stresses into these three types can be written in additive form, namely:

$$\sigma^{\text{total}} = \sigma^{\text{I}} + \sigma^{\text{II}} + \sigma^{\text{III}} \quad (12)$$

At each IP, the total stress (Types I+II+III) in the loading direction can be directly collected from the simulation result. Type I stresses are those which exist over the scale of the dimension of sample or component. They are continuous over large distances and can be obtained from the macroscopic stress curve. Types II stresses are those which exist across grains due to the anisotropy of different grains or grain families and the constraints to deformation that occur between them. They are not the grain average stress here, but the fluctuation of stresses in different grains. Type III stresses are produced at the atomic level as a result of defects, dislocation motion/interaction and precipitates in materials. It can be evaluated by the fluctuation of stress in different IPs. With the knowledge of total stress, Type I and II stress, Type III stress (intragranular fluctuation) can be then calculated from the Eq. (9). Fig. 27 represents the probability density distribution of elastic strain in 10 grains and overall RVE. The corresponding normal fitting parameters are listed in Table 7. Considering the overall RVE contains a large number of grains, it is not surprising to find that the normal profile shapes of individual grains are much higher and narrower than that of the overall RVE, suggesting that the standard deviation of local elastic strain within one grain (Type III) is much smaller than that within the whole RVE (Type I). Additionally, the deviation and mean value of the strain distribution in different grains (Type II) vary significantly (up to 100% difference) from each other.

Fig. 28 illustrates the multi-scale nature of stresses within the RVE by considering the stress component in the loading direction. The RVE showed in Fig. 28 (a) was cut in half by a horizontal plane indicated by the black dashed lines. The lower half of the RVE is shown in Fig. 28 (b), with path AB created at the cut surface. The total stress profiles (Types I+II+III) in the loading direction along the path is represented by coloured dotted lines, with the colours of dots set to be identical to that of their corresponding grains according to the colour key of IPF. The coloured short solid lines are the grain level average of stresses (Type I+II) that vary between different grains, while Type I stresses are constant along the entire path. In the current study, a significant variation of stress magnitudes within one grain and among different grains is observed. Type II and III stresses are often neglected when investigating the mechanical response of engineering components having a characteristic length of millimetres. However, mechanical failures often originate at the



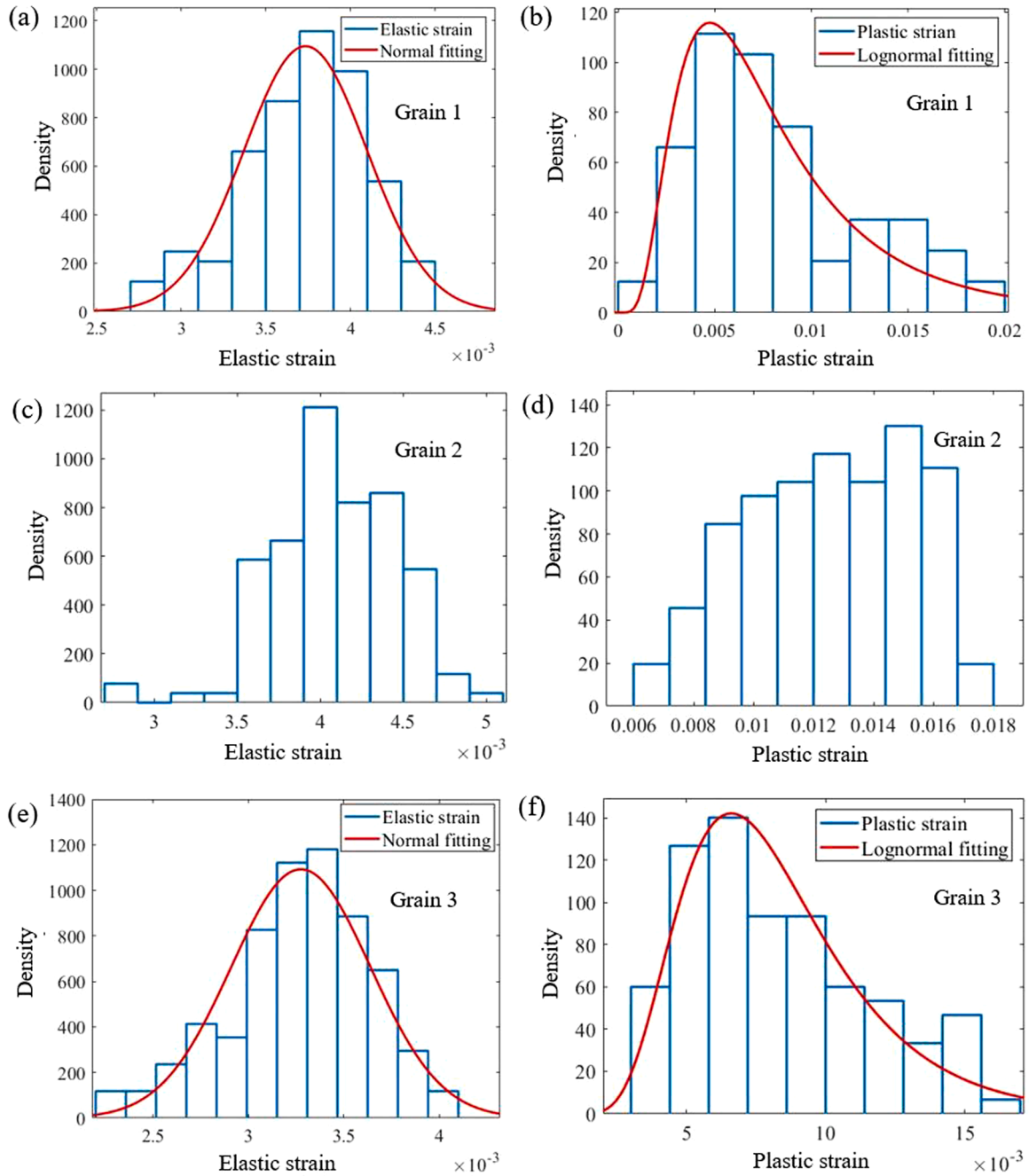


Fig. 26. The probability density distribution of elastic and plastic strains in 6 large grains.

grain level, where intragranular and intergranular stresses are critically important. For these reasons, critical assessment of stresses and strains at both macro-scale (Type I) and grain level (Type II and III) has the potential to improve the design methods for enhanced structural integrity. From the practical point of view, a detailed representation of Type II and III stresses within material microstructure remains rather computationally expensive. On the other hand, employing a statistical approach to study multi-scale stresses may allow reliable uncertainty quantification in terms of the onset and development of failure processes (Salvati and Korsunsky, 2017). It should be mentioned that the current model is not able to capture the fine-scale fluctuation of Type III stresses within the grain, as the mesh was not refined sufficiently to allow performing efficient statistical analysis of a large number of realizations.



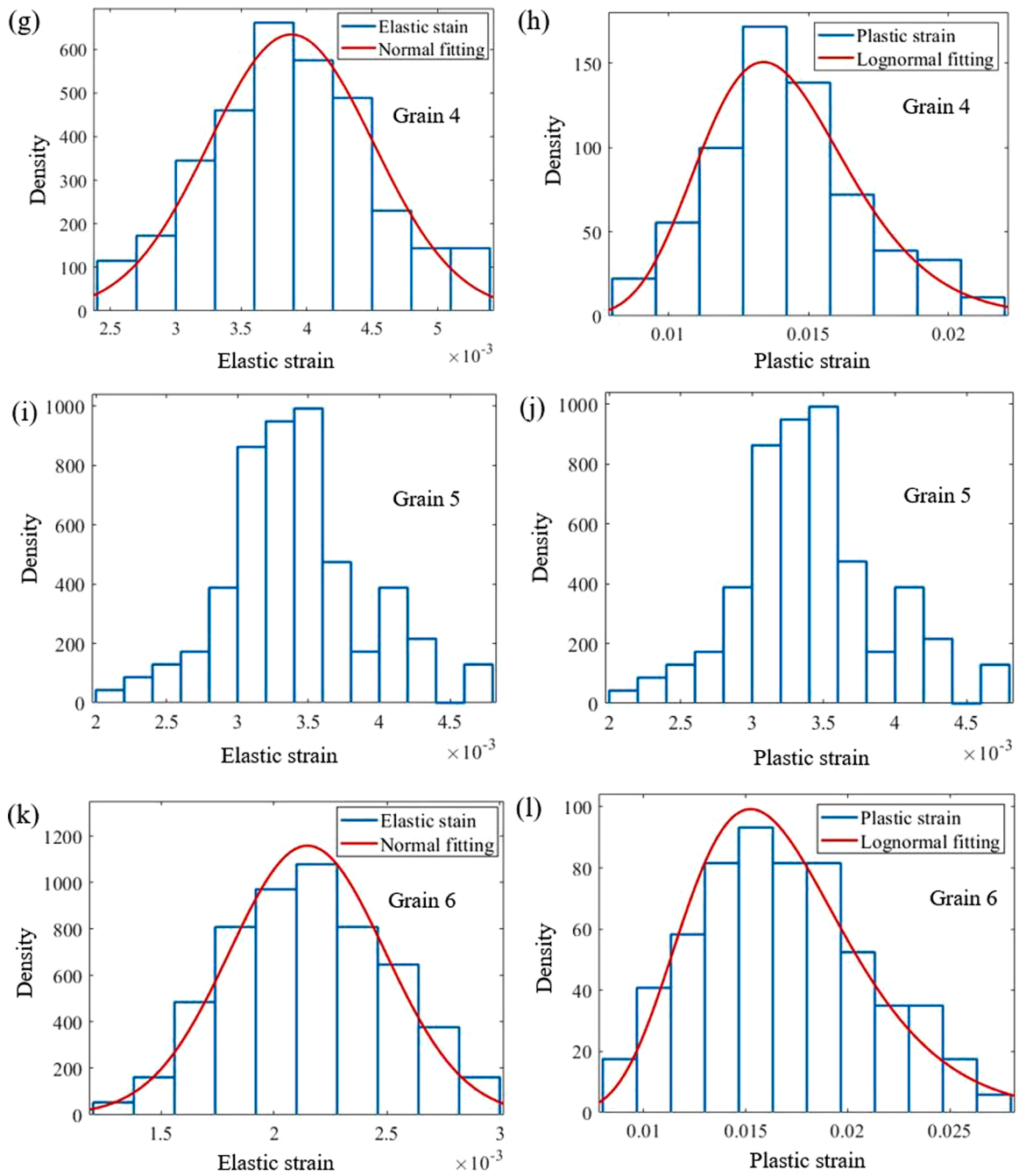


Fig. 26. (continued).

**Table 6**  
Grain and its corresponding reflection group.

Grain ID	1	2	3	4	5	6
Reflection	311	200	331	-	200	531

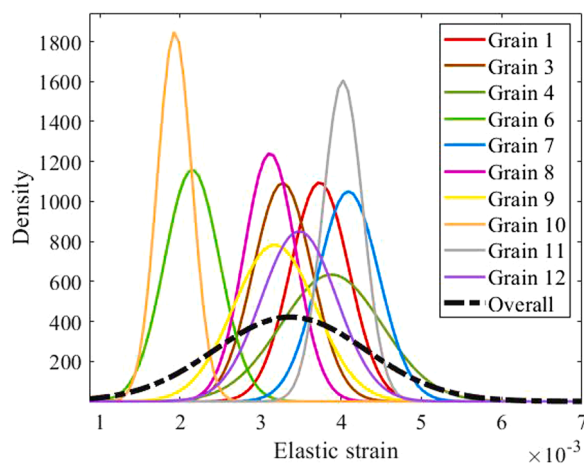


Fig. 27. A comparison of the probability density distribution of elastic strain in 10 grains and overall RVE.

Table 7

Gaussian fitting parameters of the elastic strain statistics in individual grains and overall RVE.

Elastic strain statistics	$\mu$	$\sigma$
Grain 1	3.73E-3	3.64E-4
Grain 3	3.27E-3	3.65E-4
Grain 4	3.88E-3	6.29E-4
Grain 6	2.15E-3	3.44E-4
Grain 7	4.09E-3	3.80E-4
Grain 8	3.12E-3	3.21E-4
Grain 9	3.18E-3	5.09E-4
Grain 10	1.93E-3	2.16E-4
Grain 11	4.02E-3	2.48E-4
Grain 12	3.48E-3	4.69E-4
Overall RVE	3.37E-3	9.46E-4

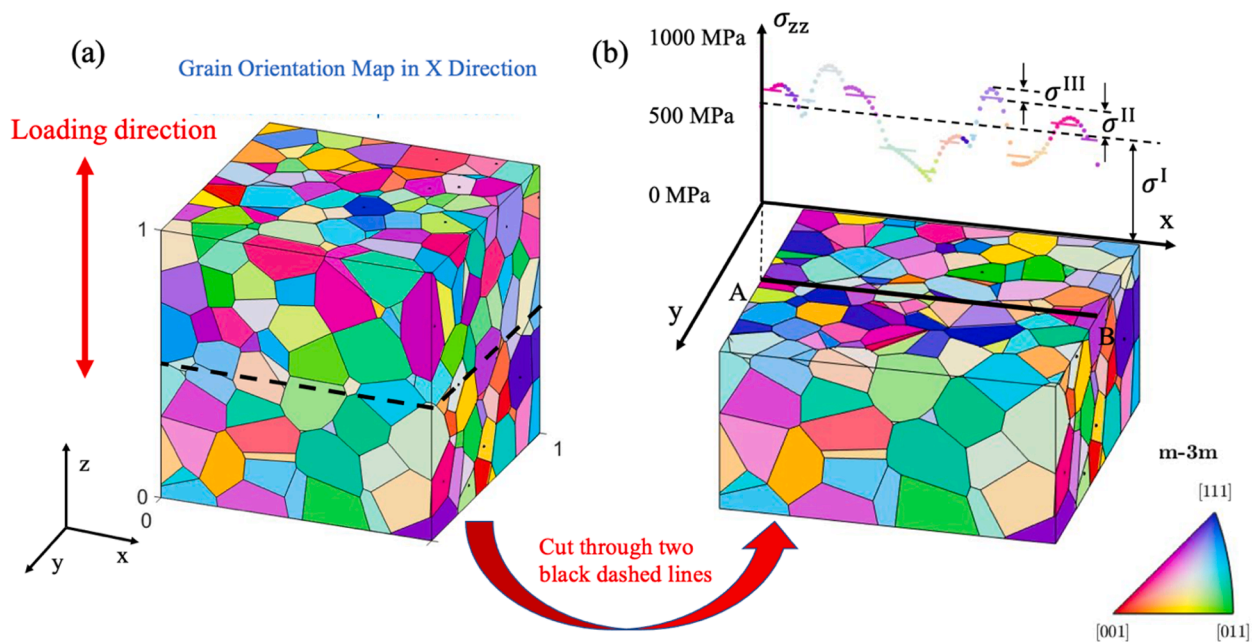


Fig. 28. Illustration of the multi-scale nature of stresses in the RVE and the separation into Types I, II and III.

## 6. The multi-scale investigation of mechanical response in two extreme realizations

Failures in structural components are often governed by extreme cases according to the weakest link principle. Therefore, it is of great importance and interest to explore the difference in macro-meso-microscopic stress and strain response for extreme realizations. Based on the stress histogram depicted in Fig. 7, two realizations No. 35 and 46 were found to behave distinctly different in terms of overall stresses at 1.55% strain. Fig. 29 represents the macroscopic stress-strain curve under uniaxial loading for realizations No. 35 and 46. Realization 35 has the highest overall stress and can be seen as the upper limit within the statistical distribution. On the other hand, Realization 46 shows the lowest overall stresses and can be looked as the lower limit. These two realizations have identical grain morphology, but different orientation permutations. Thereby, it can reasonably be assumed that the difference of overall stresses between Realizations 35 and 46 may originate from the anisotropic behaviour of different grain groups.

Fig. 30 shows the orientation-specific elastic lattice strain obtained from CPFEM diffraction post-processing for the two realizations. Analogous to their macroscopic stress-strain behaviour, the applied stress vs. elastic lattice strain curve of different grain groups (except group 331) in Realization 35 is higher than the corresponding grain groups in Realization 46. The deviation of the curves in the elastic region between these two realizations is smaller than in the near-yield region for all diffracting grain groups, indicating that the major difference of mesoscopic mechanical response comes from the anisotropic plastic deformation in different grain families. In both realizations, the applied stress and the elastic lattice strain for the 311, 220, 531 and 331 diffracting grain groups show a relatively linear correlation, while lower linearity is observed for the 111 and 200 planes. The 220 and 311 planes show less orientation dependence in the elastic region than other planes, while the highest orientation dependence is observed for 111 planes.

To capture the microscopic response of all diffracting grain groups, the distribution of elastic lattice strain in Realizations 35 and 46 across IPs that belong to different grain groups when the total strain reached near yield region (0.4% strain) are illustrated in Figs. 31 and 32, respectively. The distributions of the elastic strain for all grain groups in both realizations appear to follow a normal distribution, albeit with some asymmetry. Nevertheless, the elastic strain distributions for 111 and 200 planes could not be fitted particularly well with the normal distribution. There are mainly two explanations for the difference of local elastic strain distribution in various diffracting grain families. First, larger numbers of IPs were found to correspond to the 220, 311, 331 and 531 scattering vector orientations compared to 111 and 200 orientations. Larger data sets would result in better statistical distributions. Additionally, according to the FEDPP data illustrated in Fig. 30, the 220, 311, 331 and 531 planes show higher linearity compared to 111 and 200 planes. Strain heterogeneities increase when local behaviour becomes strongly non-linear, and when strong interaction between plastic deformation and elastic strain is observed. The lattice strain distribution is likely to be scattered and irregular if more non-linearity is apparent. The non-linearity of 111 and 200 planes suggests that strong elastic-plastic interaction occurs in grains with these two orientations. When the total strain reaches 0.4%, the material deformation undergoes the transition from elastically dominated to plastically dominated deformation, and more plastic deformation effects accumulated in 111 and 200 grain families than in the other orientations. It is therefore argued that the elastic strain distribution is greatly sensitive to the accumulated plastic slip in the elastic-plastic transition region.

Fatigue indicator parameters (FIPs) including accumulated plastic slip and dissipation energy are widely used two types of damage accumulation and fracture initiation criteria in the literature. Computable FIPs are introduced to facilitate the studies of the influence of microstructure on fatigue crack formation. It is commonly accepted that these FIPs can serve as a quantitative evaluation for the cyclic driving force for the formation and early growth of cracks within grains. High values of FIPs often corresponds to localized “hot spots” of slip. FIPs can be well associated with experimentally observed fatigue crack sites in polycrystals (Dunne and Rugg, 2008;

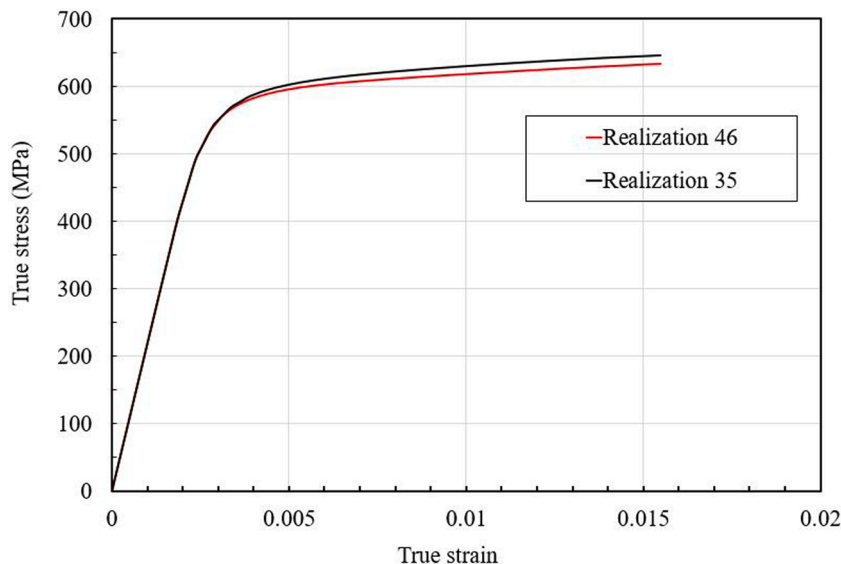


Fig. 29. Macroscopic stress-strain curves obtained from Realizations 6 and 53.

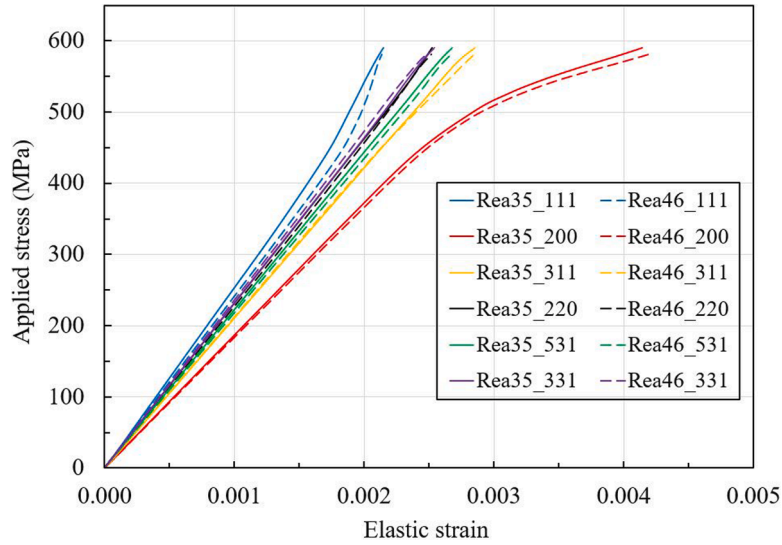


Fig. 30. Illustration of the orientation-dependent elastic lattice strain reproduced by the finite element method using Realizations 35 and 46.

Chen et al., 2018). For accumulated plastic slip, Dunne et al. found that a microstructurally sensitive crystal plasticity model can well predict the crack nucleation site based on the accumulated slip (Dunne et al., 2007). It is also suggested by some researchers that dissipated energy could be used as a FIP to determine the damage accumulation (Skelton et al., 1998; Korsunsky et al., 2007; Yuan et al., 2020). The multi-scale stress and elastic strain distributions described above provide a statistical description of the inhomogeneity of deformation in two distinctly different realizations. Ductile fracture often occurs in the region with highly localized plasticity, and this suggests the importance of physically-based initiation criteria at the microscopic level when evaluating the durability of components and structures. The plastic strain  $\varepsilon_f$  to failure in uniaxial tensile loading can be calculated using the path integral

$$\varepsilon_f = \int \sqrt{\frac{2}{3} d\epsilon_{ij}^p d\epsilon_{ij}^p} \quad (13)$$

Fig. 33 represents the distribution of accumulated plastic slip across all IPs in Realizations 35 and 46 at the total uniaxial tensile strain of 1.55%. The macroscopic strain in both realizations is expected to be the same, whereas the localized plastic strain has apparently different distributions. The maximum plastic strain in Realization 46 is 5.74%, which is slightly larger than the peak plastic strain of 5.68% in Realization 35. This implies that more localized damage is introduced in Realization 46 under uniaxial tensile loading based on the accumulated plastic slip criterion.

Energy-based criteria, such as the net dissipated energy, are often used to analyse the fatigue damage caused by cyclic loading. The increment of dissipated energy at each load increment can be expressed as

$$dW(x) = \sum_{\alpha=1}^n \tau_c^\alpha \dot{\gamma}^\alpha dt \quad (14)$$

Here  $x$  is the location of the integration point, and  $dt$  refers to the duration of load increment. The dissipated energy at each IP can be calculated by integrating Eq. (11) and summing over all increments during loading. Cyclic simulation has been carried out at room temperature on Realizations 35 and 46 for fully reversed strain-controlled loading with zero mean strain. The maximum strain was chosen to be 0.8% so that the plastic deformation was not greatly dominant, corresponding too low to intermediate cycle fatigue regime. The cyclic stress-strain response of the two realizations is depicted in Fig. 34. At the end of one cycle of loading, the local dissipation energy value across all the IPs was collected and analysed statistically. The distribution of the dissipated energy across all IPs in two realizations is illustrated in Fig. 35. Realization 35 has a larger averaged dissipated energy (13.0 mJ) after cyclic loading compared to Realization 46 (8.1 mJ), which can be explained by the fact that Realization 35 has a higher overall stress response than Realization 46 at the same strain level. The maximum dissipation energy in Realization 46 (25.3 mJ) is much smaller than that in Realization 35 (31.6 mJ). This suggests that localized failure is more likely to occur in Realization 35 under cyclic loading based on the dissipated energy criterion.

## 7. Analysis and conclusion

Stress and deformation in polycrystalline materials are often heterogeneous, and they can be classified into three types according to their characteristic length scale and controlling microstructure: Type I macroscale (different RVEs), Type II mesoscale (grains and

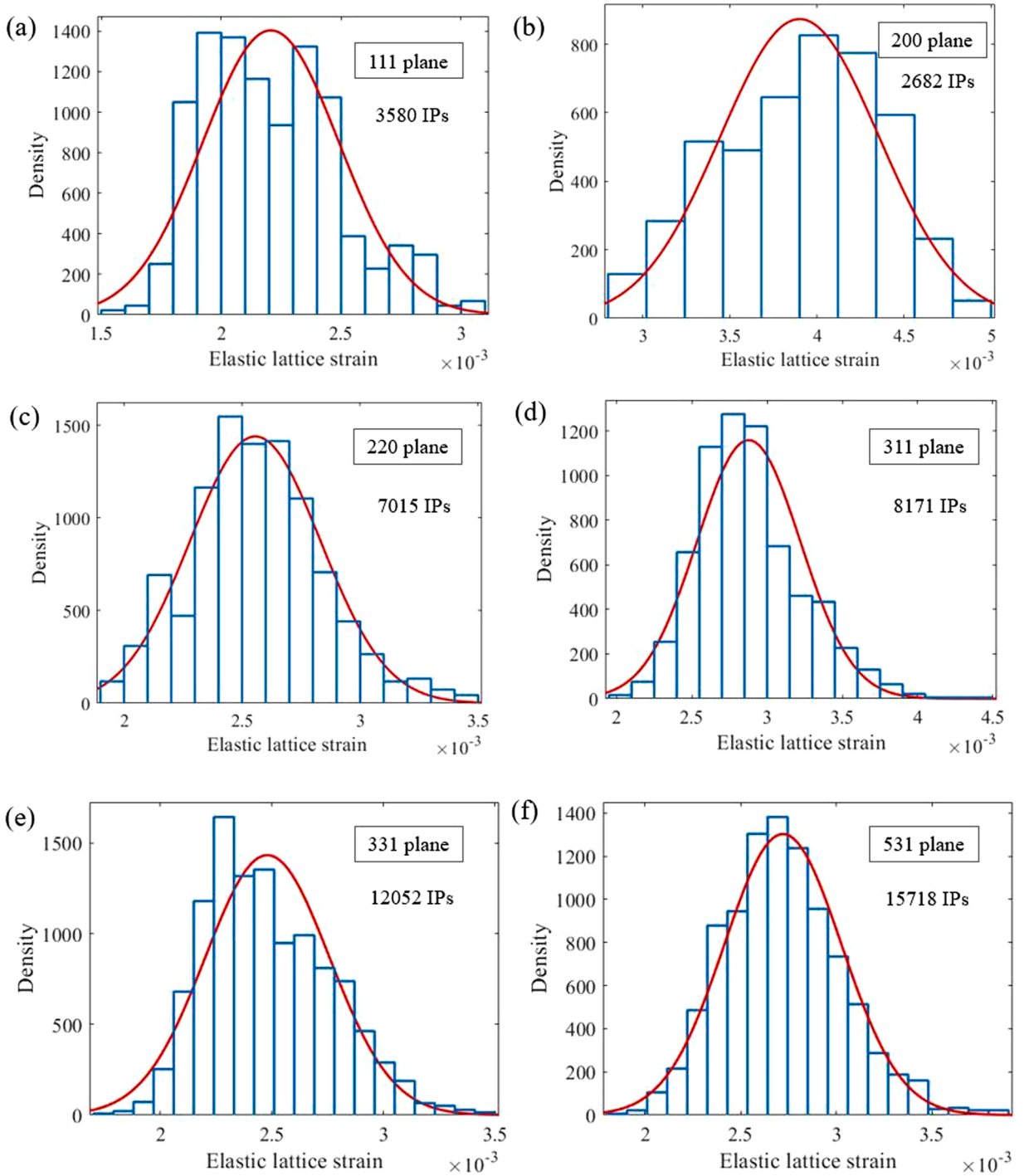


**Fig. 31.** The distribution of elastic strain in Realization 35 across the IPs that contribute to different diffraction planes at the total strain level of 0.4%.

grain groups), and Type III microscale (integration points). In the present study, a rate-independent formulation is implemented within a crystal plasticity framework utilizing representative volume elements. To perform a multiscale analysis of the distributions of strain, stress and other mechanical responses, many RVE realizations with different grain morphologies and orientation permutations were generated. The material properties and crystallographic orientation for polycrystalline alloy Haynes 282 were assigned to each integration point within an RVE such that the mesoscopic response of diffraction grain groups and microscopic behaviour across IPs could be readily captured.

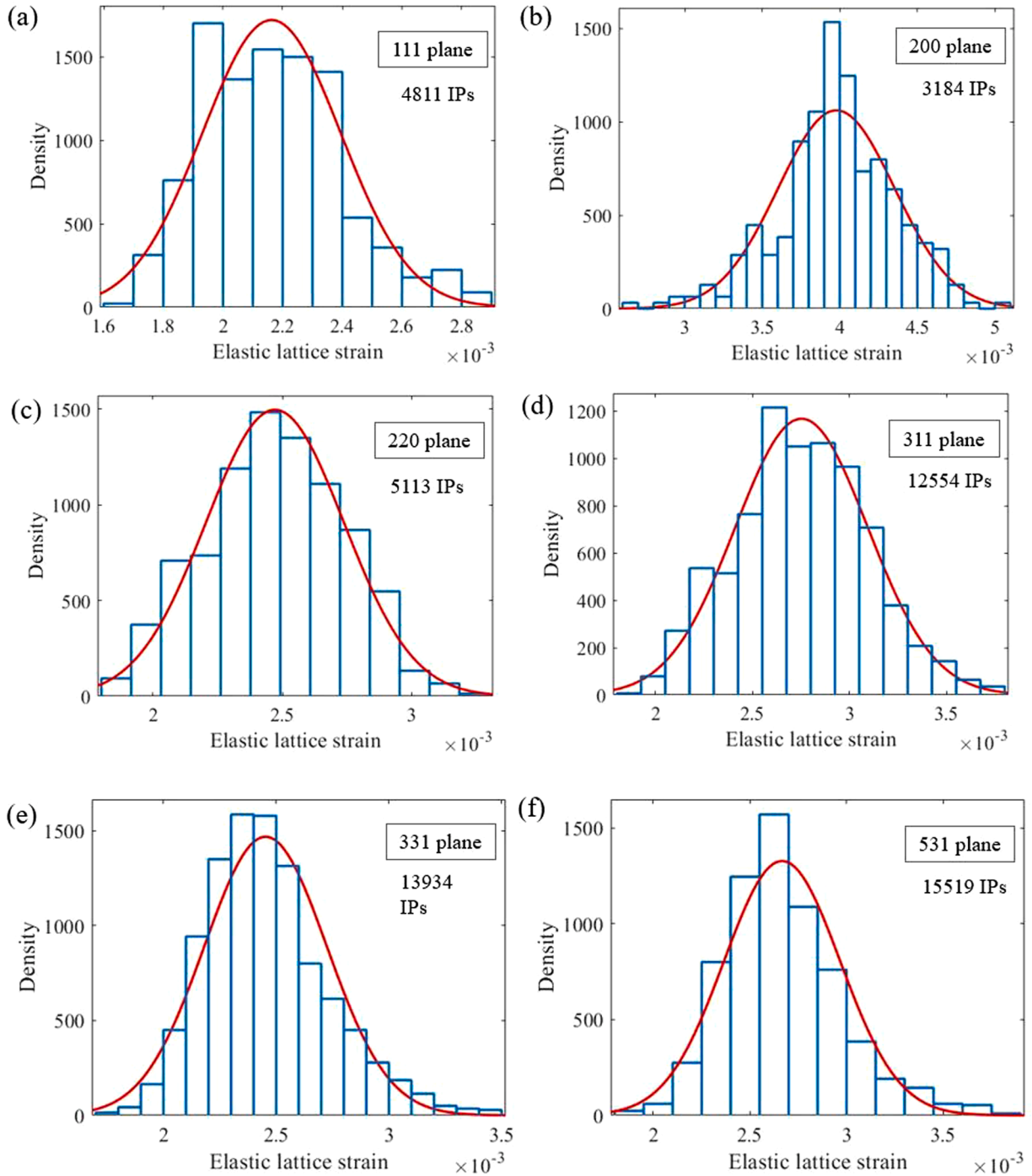


**Fig. 32.** The distribution of elastic strain in realization 46 across the IPs that contribute to different diffraction planes with a total strain level of 0.4%.

At the macroscale, the strain and stress differences emerge between different RVEs with various microstructures. Statistical analysis was performed on the macroscopic stress-strain responses of RVEs. An apparent discontinuity between elastic and plastic regimes was found in the standard deviation curve for the first set of RVEs (No. 1–48) with the same grain morphology. By changing the grain orientation permutation, the overall stresses that correspond to 1.55% strain among different RVEs were found to follow a normal distribution. The width and height of the normal distribution were affected by the parameters that described the lognormal grain size distribution. Interestingly, the morphology with a larger grain size dispersion was found to lead to smaller overall stress discrepancies. The investigation between ensembles with different grain size suggests that discretization can introduce Hall–Petch like size effect in



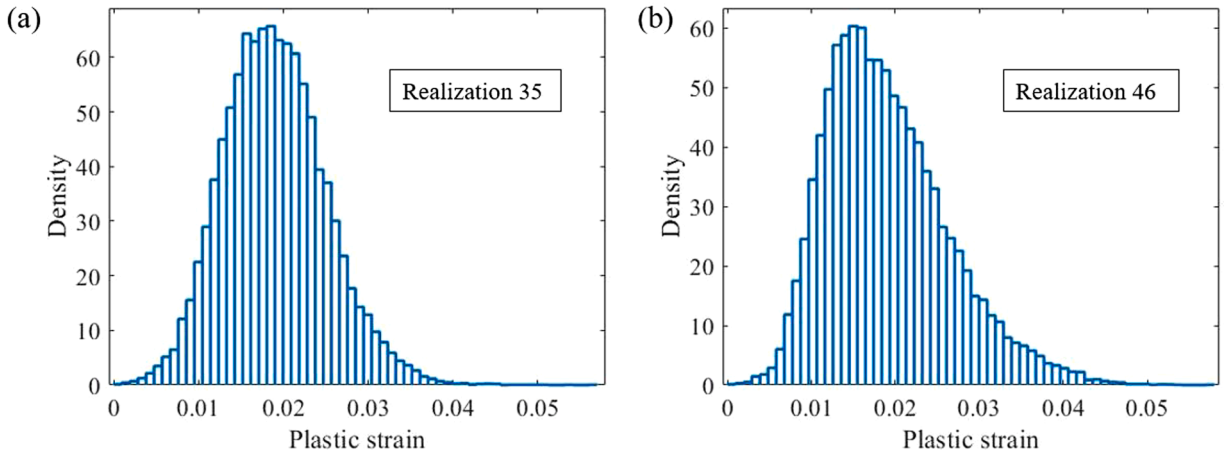


Fig. 33. The distribution of accumulated plastic slip across all IPs in two extreme realizations at a total strain of 1.55%.

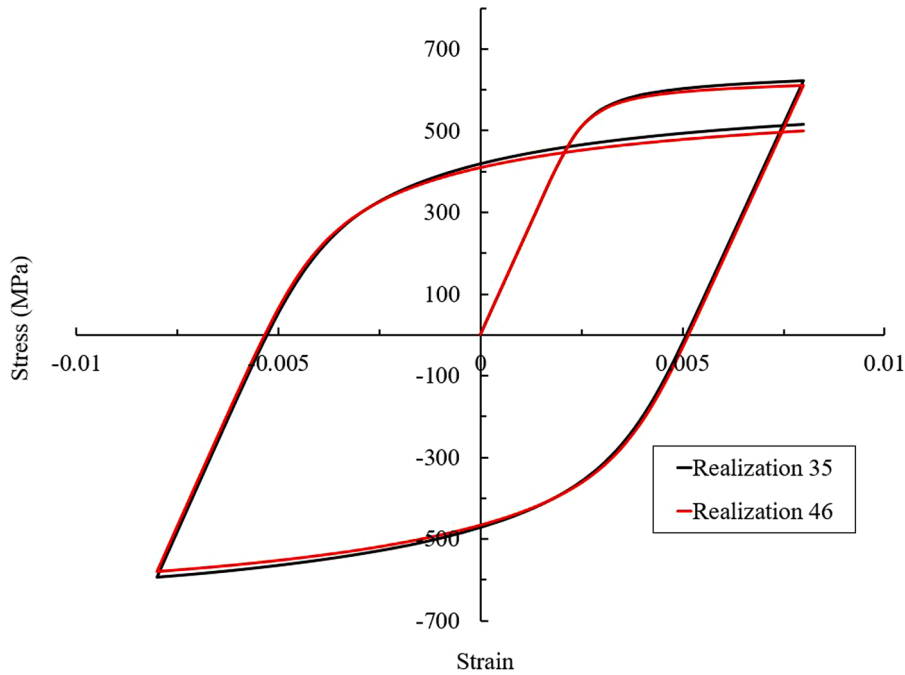


Fig. 34. The cyclic stress-strain response of realization 35 and 46 (maximum strain 0.8%).

polycrystalline materials. The overall stresses of Morphologies 3 and 8 show two distinctly different normal distribution shapes. In engineering design, the reproducibility of the mechanical behaviour of mass-produced components remains a critical question. Components with a narrower stress distribution (such as Morphology 3) are expected to be more reliable for the purposes of structural integrity, whereas parts that show a wider stress distribution (like Morphology 8) will possibly introduce a larger uncertainty for structural integrity lifing procedures.

At the mesoscopic scale, the inhomogeneous deformation is characterized by the anisotropic response that originates from different grain families. This research evaluates the grain-orientation average of elastic lattice strain via the use of diffraction post-processing of FE simulation results. The orientation-specific elastic strains reproduced by CPFEM are validated by comparison with the neutron diffraction data of a polycrystalline Haynes 282 alloy.

At the microscale, deformation is controlled by the crystal structure, defect distribution and dislocation motion/interaction, which are discrete in nature. Consequently, the stress and strain can only be obtained by averaging atomic-scale properties over a certain region (i.e. integration points in this study). When the total strain reaches 1.55%, the elastic strain (and stress) accumulation is found to be additive leading to a normal distribution, whereas plastic strain can be well described by a lognormal distribution and obeys a multiplicative accumulation process. As opposed to the distribution of local properties, the macroscopic overall stresses of different

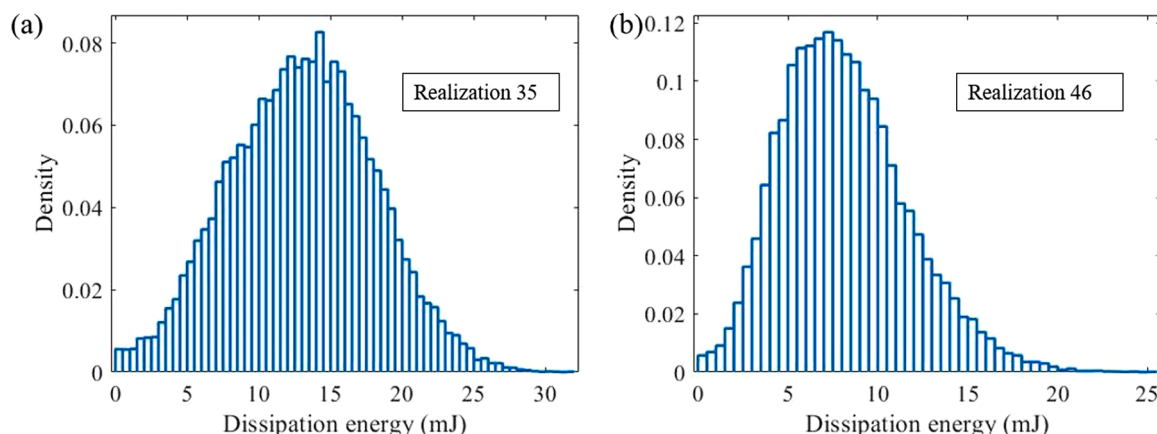


Fig. 35. Distribution of dissipation energy across all IPs in two extreme realizations at the end of cyclic loading.

RVEs follow a much narrower normal distribution. Relatively stable macroscopic stress responses of the RVEs with various grain orientation permutations and morphologies are all found to be within 2% difference bounds. The separation of stresses into these three types is illustrated using one randomly selected realization, and a significant variation of stress magnitudes within one grain (Type III) and among different grains (Type II) is observed. The above finding reveals the nature of stress and strain inhomogeneity at different scales and highlights the fact that the dispersion of local stress and strain distribution is much larger than the macroscopic average. We hypothesize that this finding is valid when the volume of interest is above a minimum representative volume that accounts for the macroscopic homogeneity of deformation.

A multiscale investigation of mechanical response is performed on two extreme realizations. Realization 35 and 46 have identical grain morphology but different orientation permutation. Realization 35 has the highest macroscopic stress-strain curve, whilst Realization 46 represents the strongest strain hardening and hence the lowest macroscopic curve. Similar to their macroscopic response, elastic lattice strains of different grain families (except the 331 group) in Realization 35 are higher than the corresponding grain families in Realization 46 at the same applied stress. The mechanical response of the 111 plane family shows the largest discrepancy between these two realizations, therefore, it is reasonable to expect the 111 plane family response to be highly orientation dependent. Microscopically, the elastic lattice strains at IPs that contribute to the 220, 311, 331 and 531 grain groups (with higher mesoscopic linearity) appear to follow more closely a Gaussian distribution in both realizations. The distributions of local plastic slip and dissipation energy suggest that pure macroscopic response is not sufficient to perform a reliable calculation for lifing analysis, as failures often originate from localized regions where microscopic behaviour with broader histograms is dominant. The above statistical analysis of stress and strain at the local and global level for different RVEs provides a means of developing new insights into the relationship between microstructure and mechanical properties at multiple scales. The results obtained here provide a statistical description of the magnitude of grain level stresses and strains variation that gives guidance to the rational design for structural integrity allowing for reliable uncertainty quantification.

#### Data availability statement

The datasets used and/or analysed during the current study are available from the corresponding author on reasonable request.

#### CRediT authorship contribution statement

**Jingwei Chen:** Conceptualization, Methodology, Validation, Formal analysis, Investigation, Writing – original draft, Writing – review & editing, Visualization. **Zifan Wang:** Methodology, Investigation, Writing – review & editing. **Alexander M. Korsunsky:** Conceptualization, Methodology, Writing – review & editing, Resources, Supervision, Project administration.

#### Declaration of Competing Interest

The authors declare that they have no known competing financial interests or personal relationships that could have appeared to influence the work reported in this paper.

#### Acknowledgements

The authors would like to acknowledge the use of the University of Oxford Advanced Research Computing (ARC) facility in carrying out this work.

## References

- Abd El-Aty, A., Xu, Y., Ha, S., Zhang, S.H., 2018. Computational homogenization of tensile deformation behaviors of a third generation Al-Li alloy 2060-T8 using crystal plasticity finite element method. *Mater. Sci. Eng. A* 731, 583–594. <https://doi.org/10.1016/j.msea.2018.06.088>.
- Alleman, C.N., Foulk, J.W., Mota, A., Lim, H., Littlewood, D.J., 2018. Concurrent multiscale modeling of microstructural effects on localization behavior in finite deformation solid mechanics. *Comput. Mech.* 61 (1), 207–218. <https://doi.org/10.1007/s00466-017-1481-5>.
- Berbenni, S., Favier, V., Berveiller, M., 2007a. Impact of the grain size distribution on the yield stress of heterogeneous materials. *Int. J. Plast.* 23 (1), 114–142. <https://doi.org/10.1016/j.ijplas.2006.03.004>.
- Berbenni, S., Favier, V., Berveiller, M., 2007b. Micro-macro modelling of the effects of the grain size distribution on the plastic flow stress of heterogeneous materials. *Comput. Mater. Sci.* 39 (1), 96–105. <https://doi.org/10.1016/j.commatsci.2006.02.019>.
- Bilger, N., Auslender, F., Bornert, M., Michel, J.C., Moulinec, H., Suquet, P., Zaoui, A., 2005. Effect of a nonuniform distribution of voids on the plastic response of voided materials: a computational and statistical analysis. *Int. J. Solids Struct.* 42 (2), 517–538. <https://doi.org/10.1016/j.jsoistr.2004.06.048>.
- Chen, B., Jiang, J., Dunne, F.P., 2018. Is stored energy density the primary meso-scale mechanistic driver for fatigue crack nucleation? *Int. J. Plast.* 101, 213–229. <https://doi.org/10.1016/j.ijplas.2017.11.005>.
- Chen, J., Korsunsky, A.M., 2021. Why is local stress statistics normal, and strain lognormal? *Mater. Des.* 198, 109319. <https://doi.org/10.1016/j.matdes.2020.109319>.
- Chen, J., Salvati, E., Uzun, F., Papadakis, C., Wang, Z., Everaerts, J., Korsunsky, A.M., 2020. An experimental and numerical analysis of residual stresses in a TIG weldment of a single crystal nickel-base superalloy. *J. Manuf. Process.* 53 (5), 190–200. <https://doi.org/10.1016/j.jmapro.2020.02.007>.
- Chen, L., Liu, W., Song, L., 2021. A multiscale investigation of deformation heterogeneity in additively manufactured 316L stainless steel. *Mater. Sci. Eng. A*, 141493. <https://doi.org/10.1016/j.msea.2021.141493>.
- Cheong, K.S., Busso, E.P., 2004. Discrete dislocation density modelling of single phase FCC polycrystal aggregates. *Acta Mater.* 52 (19), 5665–5675. <https://doi.org/10.1016/j.actamat.2004.08.044>.
- Daoud, M., Jomaa, W., Chatelain, J.F., Bouzid, A., 2015. A machining-based methodology to identify material constitutive law for finite element simulation. *Int. J. Adv. Manuf. Technol.* 77 (9–12), 2019–2033. <https://doi.org/10.1007/s00170-014-6583-z>.
- Dautria, J., Bornert, M., Gland, N., Dimanov, A., Raphanel, J., 2011. Localized deformation induced by heterogeneities in porous carbonate analysed by multi-scale digital image correlation. *Tectonophysics* 503 (1–2), 100–116. <https://doi.org/10.1016/j.tecto.2010.09.025>.
- Diard, O., Leclercq, S., Rousselier, G., Caillaud, G., 2005. Evaluation of finite element based analysis of 3D multycrystalline aggregates plasticity Application to crystal plasticity model identification and the study of stress and strain fields near grain boundaries. *Int. J. Plast.* 21 (4), 691–722. <https://doi.org/10.1016/j.ijplas.2004.05.017>.
- Dini, D., Korsunsky, A.M., Dunne, F.P., 2006. Diffraction post-processor for polycrystalline plasticity modelling. *Mater. Sci. Forum* 524, 427–432. <https://doi.org/10.4028/www.scientific.net/MSF.524.427>.
- Drugan, W.J., Willis, J.R., 1996. A micromechanics-based nonlocal constitutive equation and estimates of representative volume element size for elastic composites. *J. Mech. Phys. Solids* 44 (4), 497–524. [https://doi.org/10.1016/0022-5096\(96\)00007-5](https://doi.org/10.1016/0022-5096(96)00007-5).
- Dunne, F.P.E., Rugg, D., 2008. On the mechanisms of fatigue facet nucleation in titanium alloys. *Fatigue Fract. Eng. Mater. Struct.* 31 (11), 949–958. <https://doi.org/10.1111/j.1460-2695.2008.01284.x>.
- Dunne, F.P.E., Wilkinson, A.J., Allen, R., 2007. Experimental and computational studies of low cycle fatigue crack nucleation in a polycrystal. *Int. J. Plast.* 23 (2), 273–295. <https://doi.org/10.1016/j.ijplas.2006.07.001>.
- Esmailpour, R., Kim, H., Park, T., Pourboghra, F., Xu, Z., Mohammed, B., Abu-Farha, F., 2018. Calibration of barlat Yld2004-18P yield function using CPFEM and 3D RVE for the simulation of single point incremental forming (SPIF) of 7075-O aluminum sheet. *Int. J. Mech. Sci.* 145, 24–41. <https://doi.org/10.1016/j.jimecsci.2018.05.015>.
- Farooq, H., Caillaud, G., Forest, S., Ryckelynck, D., 2020. Crystal plasticity modeling of the cyclic behavior of polycrystalline aggregates under non-symmetric uniaxial loading: Global and local analyses. *Int. J. Plast.* 126, 102619. <https://doi.org/10.1016/j.ijplas.2019.10.007>.
- Gitman, I.M., Askes, H., Sluys, L.J., 2007. Representative volume: existence and size determination. *Eng. Fract. Mech.* 74 (16), 2518–2534. <https://doi.org/10.1016/j.engfractmech.2006.12.021>.
- Groeber, M.A., Jackson, M.A., 2014. DREAM. 3D: a digital representation environment for the analysis of microstructure in 3D. *Integr. Mater. Manuf. Innov.* 3 (1), 56–72. <https://doi.org/10.1186/2193-9772-3-5>.
- Groma, I., Bako, B., 1998. Probability distribution of internal stresses in parallel straight dislocation systems. *Physical Review B*. <https://doi.org/10.1103/PhysRevB.58.2969>.
- Hill, R., 1963. Elastic properties of reinforced solids: Some theoretical principles. *J. Mech. Phys. Solids* 11 (5), 357–372. [https://doi.org/10.1016/0022-5096\(63\)90036-X](https://doi.org/10.1016/0022-5096(63)90036-X).
- Jaladurgam, N.R., Li, H., Kelleher, J., Persson, C., Steuwer, A., Colliander, M.H., 2020. Microstructure-dependent deformation behaviour of a low  $\gamma'$  volume fraction Ni-base superalloy studied by *in-situ* neutron diffraction. *Acta Mater.* 183, 182–195. <https://doi.org/10.1016/j.actamat.2019.11.003>.
- Jiang, J., Britton, T.B., Wilkinson, A.J., 2013. Evolution of dislocation density distributions in copper during tensile deformation. *Acta Mater.* 61 (19), 7227–7239. <https://doi.org/10.1016/j.actamat.2013.08.027>.
- Kanit, T., Forest, S., Galliet, I., Mounoud, V., Jeulin, D., 2003. Determination of the size of the representative volume element for random composites: statistical and numerical approach. *Int. J. Solids Struct.* 40 (13–14), 3647–3679. [https://doi.org/10.1016/S0020-7683\(03\)00143-4](https://doi.org/10.1016/S0020-7683(03)00143-4).
- Kapetanou, O., Weygand, D., Zaiser, M., 2015. Stress and strain fluctuations in plastic deformation of crystals with disordered microstructure. *J. Stat. Mech. Theory Exp.* 2015 (8), P08009. <https://doi.org/10.1088/1742-5468/2015/08/P08009/meta>.
- Korsunsky, A.M., Dini, D., Dunne, F.P., Walsh, M.J., 2007. Comparative assessment of dissipated energy and other fatigue criteria. *Int. J. Fatigue* 29 (9–11), 1990–1995. <https://doi.org/10.1016/j.ijfatigue.2007.01.007>.
- Kotha, S., Ozturk, D., Ghosh, S., 2019. Parametrically homogenized constitutive models (PHCMs) from micromechanical crystal plasticity FE simulations, part I: Sensitivity analysis and parameter identification for Titanium alloys. *Int. J. Plast.* 120, 296–319. <https://doi.org/10.1016/j.ijplas.2019.05.008>.
- Li, Y., Wu, G., Wang, G., 2020. Micro-plastic fatigue damage mechanism governing shape instability behavior. *Int. J. Fatigue* 131, 105386. <https://doi.org/10.1016/j.ijfatigue.2019.105386>.
- Lim, H., Battaille, C.C., Bishop, J.E., Foulk, J.W., 2019. Investigating mesh sensitivity and polycrystalline RVEs in crystal plasticity finite element simulations. *Int. J. Plast.* 121, 101–115. <https://doi.org/10.1016/j.ijplas.2019.06.001>.
- Manonukul, A., Dunne, F.P.E., 2004. High- and low-cycle fatigue crack initiation using polycrystal plasticity. *Proc. R. Soc. A Math. Phys. Eng. Sci.* 460 (2047), 1881–1903. <https://doi.org/10.1098/rspa.2003.1258>.
- Min, K.M., Jeong, W., Hong, S.H., Lee, C.A., Cha, P.R., Han, H.N., Lee, M.G., 2020. Integrated crystal plasticity and phase field model for prediction of recrystallization texture and anisotropic mechanical properties of cold-rolled ultra-low carbon steels. *Int. J. Plast.* 127, 102644. <https://doi.org/10.1016/j.ijplas.2019.102644>.
- Moghaddam, M.G., Achuthan, A., Bednarczyk, B.A., Arnold, S.M., Pineda, E.J., 2017. Grain size-dependent crystal plasticity constitutive model for polycrystal materials. *Mater. Sci. Eng. A* 703, 521–532. <https://doi.org/10.1016/j.msea.2017.07.087>.
- Omairey, S.L., Dunning, P.D., Sriramula, S., 2019. Development of an ABAQUS plugin tool for periodic RVE homogenisation. *Eng. Comput.* 35 (2), 567–577. <https://doi.org/10.1007/s00366-018-0616-4>.
- Peirce, D., Asaro, R.J., Needleman, A., 1982. An analysis of nonuniform and localized deformation in ductile single crystals. *Acta Metall.* 30 (6), 1087–1119. [https://doi.org/10.1016/0001-6160\(82\)90005-0](https://doi.org/10.1016/0001-6160(82)90005-0).
- Peirce, D., Asaro, R.J., Needleman, A., 1983. Material rate dependence and localized deformation in crystalline solids. *Acta Metall.* 31 (12), 1951–1976. [https://doi.org/10.1016/0001-6160\(83\)90014-7](https://doi.org/10.1016/0001-6160(83)90014-7).
- Quested, T.E., Greer, A.L., 2004. The effect of the size distribution of inoculant particles on as-cast grain size in aluminium alloys. *Acta Mater.* 52 (13), 3859–3868. <https://doi.org/10.1016/j.actamat.2004.04.035>.

- Salvati, E., Korsunsky, A.M., 2017. An analysis of macro- and micro-scale residual stresses of type I, II and III using FIB-DIC micro-ring-core milling and crystal plasticity FE modelling. *Int. J. Plast.* 98, 123–138. <https://doi.org/10.1016/j.ijplas.2017.07.004>.
- Sarma, G.B., Dawson, P.R., 1996. Effects of interactions among crystals on the inhomogeneous deformations of polycrystals. *Acta Mater.* 44 (5), 1937–1953. [https://doi.org/10.1016/1359-6454\(95\)00309-6](https://doi.org/10.1016/1359-6454(95)00309-6).
- Shimokawa, T., Oguro, T., Tanaka, M., Higashida, K., Ohashi, T., 2014. A multiscale approach for the deformation mechanism in pearlite microstructure: Atomistic study of the role of the heterointerface on ductility. *Mater. Sci. Eng. A* 598, 68–76. <https://doi.org/10.1016/j.msea.2013.12.100>.
- Skelton, R.P., Vilhelmsen, T., Webster, G.A., 1998. Energy criteria and cumulative damage during fatigue crack growth. *Int. J. Fatigue* 20 (9), 641–649. <https://doi.org/10.1016/j.ijfatigue.2007.01.007>.
- Song, X., Hofmann, F., Korsunsky, A.M., 2010. Dislocation-based plasticity model and micro-beam Laue diffraction analysis of polycrystalline Ni foil: a forward prediction. *Philos. Mag.* 90 (30), 3999–4011. <https://doi.org/10.1080/14786435.2010.502149>.
- Song, X., Zhang, S.Y., Dini, D., Korsunsky, A.M., 2008. Finite element modelling and diffraction measurement of elastic strains during tensile deformation of HCP polycrystals. *Comput. Mater. Sci.* 44 (1), 131–137. <https://doi.org/10.1016/j.commatsci.2008.01.043>.
- Statnik, E.S., Salimon, A.I., Besnard, C., Chen, J., Wang, Z., Moxham, T., Dolbnya, I.P., Korsunsky, A.M., 2020. Ovine bone morphology and deformation analysis using synchrotron X-ray imaging and scattering. *Quantum Beam Sci.* 4 (3), 29. <https://doi.org/10.3390/qbs4030029>.
- Stopka, K.S., Gu, T., McDowell, D.L., 2020. Effects of algorithmic simulation parameters on the prediction of extreme value fatigue indicator parameters in duplex Ti-6Al-4V. *Int. J. Fatigue* 141, 105865. <https://doi.org/10.1016/j.ijfatigue.2020.105865>.
- Tang, A., Liu, H., Liu, G., Zhong, Y., Wang, L., Lu, Q., Wang, J., Shen, Y., 2020. Lognormal distribution of local strain: a universal law of plastic deformation in material. *Phys. Rev. Lett.* 124 (15), 1–6. <https://doi.org/10.1103/PhysRevLett.124.155501>.
- Trias, D., Costa, J., Turon, A., Hurtado, J.E., 2006. Determination of the critical size of a statistical representative volume element (SRVE) for carbon reinforced polymers. *Acta Mater.* 54 (13), 3471–3484. <https://doi.org/10.1016/j.actamat.2006.03.042>.
- Tucker, J.C., Chan, L.H., Rohrer, G.S., Groeber, M.A., Rollett, A.D., 2012. Tail departure of log-normal grain size distributions in synthetic three-dimensional microstructures. *Metall. Mater. Trans. A* 43 (8), 2810–2822. <https://doi.org/10.1007/s11661-011-0851-4>.
- Wang, Z., Chen, J., Besnard, C., Korsunsky, A.M., 2020a. Microstructure evolution in a severely cold-worked NiTi wire during ageing treatment: an *in situ* neutron diffraction study. *Mater. Lett.* 281, 128676. <https://doi.org/10.1016/j.matlet.2020.128676>.
- Wang, Z., Chen, J., Besnard, C., Kuncicka, L., Kocich, R., Korsunsky, A.M., 2020b. *In situ* neutron diffraction investigation of texture-dependent Shape Memory Effect in a near equiatomic NiTi alloy. *Acta Mater.* 202, 135–148. <https://doi.org/10.1016/j.actamat.2020.10.049>.
- Xue, R., Wang, X., Yang, Q., Xu, D., Sun, Y., Zhang, J., Krishnaswamy, S., 2021. Grain size distribution characterization of aluminum with a particle swarm optimization neural network using laser ultrasonics. *Appl. Acoust.* 180, 108125. <https://doi.org/10.1016/j.apacoust.2021.108125>.
- Yuan, G.J., Zhang, X.C., Chen, B., Tu, S.T., Zhang, C.C., 2020. Low-cycle fatigue life prediction of a polycrystalline nickel-base superalloy using crystal plasticity modelling approach. *J. Mater. Sci. Technol.* 38, 28–38. <https://doi.org/10.1016/j.jmst.2019.05.072>.
- Zhang, K., Holmedal, B., Hopperstad, O.S., Dumoulin, S., Gawad, J., Van Bael, A., Van Houtte, P., 2015. Multi-level modelling of mechanical anisotropy of commercial pure aluminium plate: crystal plasticity models, advanced yield functions and parameter identification. *Int. J. Plast.* 66, 3–30. <https://doi.org/10.1016/j.ijplas.2014.02.003>.
- Zhang, K., Holmedal, B., Manik, T., Saai, A., 2019. Assessment of advanced Taylor models, the Taylor factor and yield-surface exponent for FCC metals. *Int. J. Plast.* 114, 144–160. <https://doi.org/10.1016/j.ijplas.2018.10.015>.